

A Deep 1.2 mm Map of the Lockman Hole North Field

R. R. Lindner¹, A. J. Baker¹, A. Omont², A. Beelen³, F. N. Owen⁴, F. Bertoldi⁵, H. Dole^{3,6}, N. Fiolet^{2,3}, A. I. Harris⁷, R. J. Ivison⁸, C. J. Lonsdale⁹, D. Lutz¹⁰, & M. Polletta¹¹

ABSTRACT

We present deep 1.2 mm continuum mapping of a 566 arcmin² area within the Lockman Hole North field, previously a target of the *Spitzer* Wide-area Infrared Extragalactic (SWIRE) survey and extremely deep 20 cm mapping with the Very Large Array, which we have obtained using the Max-Planck millimeter bolometer (MAMBO) array on the IRAM 30 m telescope. After filtering, our full map has an RMS sensitivity ranging from 0.45 to 1.5 mJy beam⁻¹, with an average of 0.75 mJy beam⁻¹. Using the pixel flux distribution in a map made from our best data, we determine the shape, normalization, and approximate flux density cutoff for 1.2 mm number counts well below our nominal sensitivity and confusion limits. After validating our full dataset through comparison with this map, we successfully detect 41 1.2 mm sources with S/N > 4.0 and $S_{1.2\text{ mm}} \simeq 2 - 5$ mJy. We use the most significant of these detections to directly determine the integral number counts down to 1.8 mJy, which are consistent with the results of the pixel flux distribution analysis. 93% of our 41 individual detections have 20 cm counterparts, 49% have *Spitzer*/MIPS 24 μ m counterparts, and one may have a significant *Chandra* X-ray counterpart. We resolve $\simeq 3\%$ of the cosmic infrared background (CIB) at 1.2 mm into significant detections, and directly estimate a 0.05 mJy faint-end cutoff for the counts that is consistent with the full intensity of the 1.2 mm CIB. The median redshift of our 17 detections with spectroscopic or robust photometric redshifts is $z_{\text{median}} = 2.3$, and rises to $z_{\text{median}} = 2.9$ when we include redshifts estimated from the radio/far-infrared spectral index. By using a nearest neighbor and angular correlation function analysis, we find evidence that our S/N > 4.0 detections are clustered at the 95% confidence level.

Subject headings: galaxies: formation — galaxies: high-redshift — galaxies: starburst — submillimeter: galaxies

¹Department of Physics and Astronomy, Rutgers, the State University of New Jersey, 136 Frelinghuysen Road, Piscataway, NJ 08854-8019; {lindner, ajbaker}@physics.rutgers.edu

²Institut d'Astrophysique de Paris, Université Pierre Marie Curie and CNRS, 98 bis boulevard Arago, 75014 Paris, France; {omont, fiolet}@iap.fr

³Institut d'Astrophysique Spatiale, Université Paris Sud 11 and CNRS, Orsay, France; {alexandre.beelen, herve.dole}@ias.u-psud.fr

⁴National Radio Astronomy Observatory, PO Box 0, Socorro, NM 87801; fowen@nrao.edu

⁵Argelander Institut für Astronomie, Auf dem Hügel 71, 53121 Bonn, Germany; bertoldi@astro.uni-bonn.de

⁶Institut Universitaire de France

⁷Department of Astronomy, University of Maryland, College Park, MD 20742-2421; harris@astro.umd.edu

⁸UK Astronomy Technology Centre, Royal Observatory,

1. Introduction

Over a decade ago, measurement of the cosmic infrared background (CIB: Puget et al. 1996; Fixsen et al. 1998) revealed that approximately half of all of the light in the universe emerges at far-infrared wavelengths due to reprocessing

Blackford Hill, Edinburgh EH9 3HJ, UK; rji@roe.ac.uk

⁹North American ALMA Science Center, National Radio Astronomy Observatory, 520 Edgemont Road, Charlottesville, VA 22903; clonsdal@nrao.edu

¹⁰Max-Planck Institut für extraterrestrische Physik, Postfach 1312, 85741 Garching, Germany; lutz@mpe.mpg.de

¹¹INAF-IASF Milano, via E. Bassini 15, 20133 Milan, Italy; polletta@lambrate.inaf.it

by dust (e.g., Dole et al. 2006). With the advent of the Submillimeter Common-User Bolometer Array (SCUBA; Holland et al. 1999), it became clear around the same time that not all of this reprocessed emission originated in galaxy populations that could be easily detected with optical telescopes. Instead, SCUBA surveys at $850\ \mu\text{m}$ revealed the existence of a population of bright submillimeter galaxies (SMGs; Smail et al. 1997; Barger et al. 1998; Hughes et al. 1998) with faint or undetectable optical counterparts. Optical spectroscopy of the least obscured members of the population (Ivison et al. 1998, 2000), followed up by detections of CO emission (Fruer et al. 1998, 1999), confirmed that SMGs were indeed a high- z population. Their faint X-ray counterparts (Alexander et al. 2003, 2005) as well as mid-infrared spectroscopy (Valiante et al. 2007; Menéndez-Delmestre et al. 2007, 2009; Pope et al. 2008) indicated that they were not predominantly powered by accretion, but rather by star formation. These observations suggest that SMGs may play an important role in the cosmic star formation history. However, the details of their star formation remain uncertain. Different schools of thought exist about whether SMGs are major mergers (e.g., Conselice et al. 2003; Narayanan et al. 2009, 2010) or host bursts triggered by the inflow of intergalactic gas along filaments (Davé et al. 2010). Likewise, galaxy evolution models that consider SMGs have disagreed on whether they are (Baugh et al. 2005) or are not (Hayward et al. 2011) forming stars with an unusually top-heavy initial mass function (IMF).

Understanding how SMGs fit into the overall history of cosmic star formation has been impeded by their high obscuration in the optical and the coarse angular resolution of the (sub)millimeter bolometer arrays used to detect them. An important advance came with the use of deep, high-resolution radio continuum maps with the Very Large Array (VLA) to localize SMGs on the basis of the far-IR/radio correlation. Keck followup of radio-preselected SMG samples (Ivison et al. 2002; Chapman et al. 2003, 2005) broke the logjam for determining SMGs' redshifts, allowing a dramatic expansion of SMG samples with CO-confirmed spectroscopic redshifts and spatially resolved maps (Neri et al. 2003; Greve et al. 2005; Tacconi et al. 2006). Al-

though these developments have been important and exciting, there are a number of caveats on the current state of our knowledge. First, not all SMGs have counterparts in VLA maps of typical depths, and not all that have counterparts yield optical spectroscopic redshifts; this has led to uncertainties in the population's overall redshift distribution, especially at the high- z end. Second, we have come to realize that the $850\ \mu\text{m}$ waveband at which the influential early SCUBA work was done does not give us a complete picture of all dusty galaxy populations at high redshift: observations at shorter/longer wavelengths preferentially detect populations with higher/lower dust temperatures and/or lower/higher redshifts (e.g., Chapman et al. 2004; Valiante et al. 2007; Magnelli et al. 2010; Chapman et al. 2010; Magdis et al. 2010). Finally, with the exception of highly lensed systems, our direct knowledge is restricted to bright individual detections for which limited sensitivity and angular resolution (vs. confusion) are not fatal obstacles. Understanding the lower- L_{IR} galaxy populations that produce the bulk of the CIB is challenging, and efforts to determine their properties are not always consistent with the CIB's normalization (e.g., Scott et al. 2010).

To fill in some of the gaps in our knowledge, we need to obtain deep mapping at multiple (sub)millimeter wavelengths, at high angular resolution, over a large area that has good multiwavelength coverage (and especially, very deep radio continuum data). This combination of properties can in principle allow us to (a) optimize the identification of counterparts at other wavelengths, and therefore the determination of redshifts and the assessment of SMGs' detailed evolutionary states; (b) defeat cosmic variance and optimize sensitivity to clustering and large-scale structure, a key first step in connecting the properties of SMGs to the properties of the dark matter halos that host them; and (c) strongly constrain the parameters of SMG number counts down to faint flux densities, so that we can accurately compare the census of obscured star formation to the constraint of the CIB.

In this paper, we report 1.2 mm observations at $11''$ resolution of a unique deep field that satisfies many of these needs. Our map is both larger and more sensitive than previous deep maps made at 1.2 mm (e.g., Greve et al. 2004;

Bertoldi et al. 2007; Greve et al. 2008), and compared to recent work done with other instruments, displays a competitive combination of attributes. Surveys made at 1.1 mm using ASTE/AzTEC have mapped equal or wider fields to a greater depth, but with much lower spatial resolution (e.g., Scott et al. 2010; Hatsukade et al. 2011). Maps using JCMT/AzTEC and APEX/LABOCA generally achieve wider fields or greater depths, but not both, and also have coarser spatial resolution (e.g., Scott et al. 2008; Perera et al. 2008; Weiß et al. 2009; Austermann et al. 2010). The powerful combination of resolution, depth, and extent of our MAMBO map, together with the rich supplementary data available for our target field, make it a powerful tool for studying the properties of SMGs.

Our map lies within the Lockman Hole North (LHN) field, centered at 10:46:00 and +59:01:00 (J2000), which was one of the targets of the *Spitzer* Wide-Area Infrared Extragalactic (SWIRE) survey (Lonsdale et al. 2003). In addition to SWIRE coverage in all four IRAC and all three MIPS bands, the LHN has been the subject of extremely deep 20 cm continuum mapping with the Very Large Array (VLA) by Owen & Morrison (2008), who produced an ABCD configuration synthesis image with a central 1σ RMS sensitivity of $2.7\ \mu\text{Jy}$. These data have been further supplemented by 90 cm VLA mapping (Owen & Morrison 2009a), 50 cm GMRT mapping (Fiolet et al. 2009; Owen et al. 2011a), deep *Spitzer* $24\ \mu\text{m}$ imaging (Owen et al. 2011b), optical spectroscopy with WIYN (Owen & Morrison 2009a), X-ray imaging from the *Chandra*/SWIRE survey (Polletta et al. 2006; Wilkes et al. 2009), and determination of photometric redshifts from multicolor optical and near-IR imaging (Strazzullo et al. 2010). The LHN is also one of the targets of the *Herschel* Multi-tiered Extragalactic Survey (HerMES; Oliver et al. 2010).

2. Observations

We used the 117-element Max-Planck millimeter bolometer (MAMBO) array (Kreysa et al. 1998) at the IRAM 30m telescope to obtain on-the-fly mapping of the LHN at an effective wavelength of 1.2 mm. Our observations were obtained over the course of five semesters from 2006 through

2010 (Table 1). Due to telescope control software problems during the first two semesters – an error in computing corrections for atmospheric refraction, which undermined the quality of the pointing during the first semester, and tracking jitter that undermined map reconstruction during both semesters – we have restricted our initial analysis (e.g., §4) to a “best” map that includes only the data from our final three semesters of observations. We have also constructed a “full” map using data from all five semesters, whose reliability we can validate based on comparison with the “best” map (§5.2), and which we therefore use for our analysis of the bright source population in the field. 101.3 hr and 192.5 hr of data were combined to produce the “best” and “full” maps with areas of $514\ \text{arcmin}^2$ and $566\ \text{arcmin}^2$, and average depths of $0.90\ \text{mJy beam}^{-1}$ and $0.75\ \text{mJy beam}^{-1}$, respectively.

During all five semesters, our MAMBO data were acquired during the weeks that IRAM dedicates to pooled observations of multiple bolometer projects. As a result, most of our data were taken with 250 GHz zenith opacity ≤ 0.3 , low sky noise, and essentially no cloud cover. Observations were limited to LST ranges when the LHN had elevation $\geq 40^\circ$ (to minimize opacity corrections and pointing anomalies) and $\leq 80^\circ$ (to avoid slewing errors and sudden accelerations of the MAMBO array). We built up coverage of our field by making many small $\sim 300'' \times 320''$ (azimuth \times elevation) maps, each of which required 41 minutes to complete. The pointing centers of these small maps were arranged in a rectangular grid with $2'$ spacings between map centers.

We planned the observations so that before (and usually after) each 41-minute map, the telescope was pointed on a nearby quasar – typically J1033+609 at a distance of 1.9° from field center, with $S_{1.2\ \text{mm}} \sim 0.3\ \text{Jy}$. Every 1–2 maps, a skydip was performed to measure the zenith opacity, confirm that weather conditions remained good, and allow the interpolation of opacity corrections during the maps themselves. Standard flux calibrators were observed roughly every four hours; these coincided with large slews, to force resets of the telescope’s inclinometers. Focus measurements on bright quasars or planets were made at the beginning of each observing session as well as after sunrise and sunset. We required all of these

calibrations so as to minimize pointing errors and anomalous refraction, as is important for the detection of faint point sources in a wide-area map.

The IRAM 30 m uses a chopping secondary mirror to subtract low-frequency sky noise from on-the-fly MAMBO maps. This chopping gives the telescope an effective double-beam point spread function (PSF) on the sky, with one positive and one negative beam separated in azimuth and symmetric about the nominal pointing center. During shift-and-add (SAA) reconstruction (see §3), negative-beam data are inverted and combined (for a given sky position) with their positive-beam counterparts. The end result is a triple-beam pattern that is a well-defined function of position for any single observation: two negative sidelobes bracket a positive beam in azimuth. The SAA algorithm thus conserves the mean flux of the observations, in that the negative sidelobes together contain as much integrated flux as the positive beam. When many observations are combined into a single mosaicked image, the effective PSF is a superposition of many triple-beam patterns that can vary substantially with position.

Since a given sky position within the LHN usually falls within several of our small maps, varying the chop throw and scan direction tends to scatter the negative flux into a uniform annulus around the positive central Gaussian, reducing its peak intensity and minimizing its deleterious effects on the fluxes of nearby pixels. We therefore (a) used different chop throws for alternating columns in our grid of pointing centers, and (b) recorded the scan direction of each map in equatorial coordinates, so that observers (to the best of their ability) could observe new grid positions at LSTs such that scan directions would not match those of (existing) adjacent maps. In the central regions of our final maps (i.e., where we extract sources), peak intensities of the negative sidelobes reach only 5% of the peak positive flux thanks to our adoption of these strategies.

During our first two semesters of observations, we obtained maps of 88 grid positions out of 100 in a 10×10 grid centered on the LHN field center stated in §1. During our last three semesters, which contribute to the “best” map, we observed 97 positions of 99 in a 9×11 grid, extending $2'$ farther east but $2'$ less far south than the original grid, as well as two additional grid locations

in the southeast corner. Between the first and second semesters, we swapped which sets of pointing centers were observed with which chop throws ($36''$ and $48''$ throws vs. $42''$ and $36''$ throws for alternating columns). Due to the differences in spatial coverage and weather conditions during the observations, the areas where the “best” map and the “full” map are respectively deepest overlap but do not match perfectly (see Figure 1).

3. Data reduction

3.1. Signal maps

The raw bolometer time stream data were reduced using Robert Zylka’s MOPSIC¹ pipeline, which is distributed in parallel with IRAM’s GILDAS package. MOPSIC is the standard package for reducing deep MAMBO on-the-fly maps (see e.g., Greve et al. 2004; Voss et al. 2006; Bertoldi et al. 2007; Greve et al. 2008). We now briefly outline the steps of the MOPSIC reduction pipeline; for further details see Greve et al. (2004). The pipeline removes spikes in the time stream data stronger than $5\times$ the instantaneous bolometer RMS noise. It also subtracts a third-order polynomial baseline in time and performs correlated signal filtering on the bolometer time streams to identify and remove foreground atmospheric emission that affects many bolometers simultaneously. Each bolometer is correlated with an annulus of neighboring bolometers within a $150''$ radius, and the average signal of the twelve most highly correlated bolometers is subtracted away. The filtered time streams are then binned into $3.5'' \times 3.5''$ pixels, and a signal map is reconstructed using the SAA algorithm. The individual signal maps are combined into a mosaic image by averaging the map flux density at each pixel weighted by the local inverse variance. Our “optimally filtered” signal map (Figure 2) was created by applying a PSF-matched filter to the final mosaic image (§5.1).

In addition to the signal map, the MOPSIC pipeline also produces a weight map that is locally proportional to the inverse variance in the signal map. By enforcing that the Gaussian distribution of the S/N map pixel distribution has a standard deviation of unity, we normalize the weight map

¹see <http://www.iram.es/IRAMES/mainWiki/CookbookMopsic>

so that it can be used to find the local RMS noise, $\sigma = 1/\sqrt{W}$, in the image (see Figure 1). Using the weight map as a guide to find the local RMS noise for a detection is more robust than using the nearby pixels themselves, because locally the pixels are affected by the negative residual sidelobes of SAA reconstruction, as well as those of other bright nearby sources.

3.2. Noise maps

Because of the telescope’s effective triple-beam PSF, each source in the field injects negative as well as positive flux into the map. To generate realizations of source-free maps, hereafter referred to as “noise maps,” we removed the negative and positive flux from undetected as well as bright sources using two different techniques. We go on to use the different results for different purposes.

We constructed the first type of noise map with a technique common in MAMBO data analysis (see, e.g., Greve et al. 2004; Bertoldi et al. 2007; Greve et al. 2008), using the data reduction pipeline to scramble the known locations of the bolometers within the image plane. During reconstruction of the time stream data, this has the effect of smearing the flux from any one source into an area on the sky of approximately 200 arcmin^2 , reducing the intensity of the source’s peak flux contributions by a factor of $\sim 10^3$ and making the peak flux contribution from our strongest sources ~ 200 times fainter than the RMS noise. Because the telescope’s chopping ensures that the mean of the map is zero, there is no residual baseline increase as the negative flux contributions are identically smoothed. These “shuffled noise maps” are simple to construct, but it is cumbersome to produce large numbers of them since each requires a full reduction of the data using the MOPSIC pipeline. Therefore, we use the shuffled noise maps only to estimate the noise of our “full” data during source extraction (§5.1) as well as in the Monte Carlo simulation of completeness (§5.5).

We needed to develop a different technique for creating noise maps in order to quickly generate thousands of independent noise realizations of chopped data for our $P(D)$ analysis. For this we subtracted subsets of the data that are “jackknifed” in the sense that we remove fractions of the original data first. One *full* image of our field is created using the data from only *one* bolome-

ter in the array at a time. All bolometers other than the one of interest are masked away after the correlated signal filter is applied, so the data still receive the benefit of correlated sky noise subtraction. Two half-sets of these images are then selected at random and subtracted from each other to produce one realization of noise. This technique is similar to the jackknifing by scan commonly used for AzTEC data (see, e.g., Scott et al. 2008, 2010; Perera et al. 2008; Austermann et al. 2010), in that each jackknifed subset uses the scanning information of every available map. Use of this information is especially important for our chopped data if we are to remove negative flux artifacts from the triple-beam PSF as well as positive flux. These “jackknifed noise maps” are more amenable to mass production, and are guaranteed to remove all contributions from a source however faint, so they are used in our pixel flux distribution (PFD) analysis (§4) and in our Monte Carlo simulations to estimate numbers of spurious detections (§5.4).

The PFDs for S/N maps created with both jackknifed and shuffled noise exhibit random Gaussian noise to high precision (Figure 3), with reduced chi-square for standard normal distribution fits of 1.0 ± 0.2 and 1.2 ± 0.2 , respectively.

3.3. Simulated maps

Our simulated sky maps are constructed by populating noise maps with simulated sources. Careful construction of these maps is important for the fluctuation analysis described below (§4), for which our method relies entirely on our ability to authentically reproduce the signal from the MAMBO array so as to faithfully reproduce the PFD. Thus, when adding sources into a noise map, we need to take into account the position-dependent negative sidelobes as well as the position-independent positive flux profile for each injected source.

To handle the varying PSF properly, we take an approach similar to that of Greve et al. (2008) and model the changes in the PSF explicitly as a function of position. We use the MOPSIC pipeline script `map_negres.mopsic`, which will calculate the expected negative residual pattern on the sky in equatorial coordinates for a given set of observations and an ideal, gridded, input source model. As an input we used an array of ideal Gaussian point source profiles, each with $11''$ FWHM, span-

ning the entire field and spaced as closely as possible without having the sidelobes overlap. This minimum spacing is set by our larger chop throw (42'' for all of our “best” data and the overwhelming majority of our “full” dataset). The result is an array showing the full PSF near any location in the map (see Figure 4). Because the $\sim 84''$ spacing is less than the 300'' extent of each individual map and the 120'' separation between map pointing centers, the PSF morphologies change slowly from one to the next. We thus generate an authentic point source response in a simulated map by using the closest available PSF relative to the position of a given injected source.

4. $P(D)$ analysis of the pixel flux distribution

We constrained the 1.2 mm number counts below our nominal sensitivity and confusion limits by performing a fluctuation analysis, also known as a $P(D)$ analysis (Condon 1974). The $P(D)$ analysis has the advantage of using information from the entire PFD of the map (see Figure 5) to constrain the number counts, rather than using only those pixels above the source detection threshold (e.g., by counting bright sources). This distinction makes the $P(D)$ analysis robust against the small number statistics of counting detections in the map. Additionally, the nature of the Monte Carlo simulation described below allows us to minimize uncertainties in flux boosting and completeness, as well as the effects of confusion and source blending, because they are built into the simulation through the injection of model sources. These benefits have led Monte Carlo simulation $P(D)$ analyses (e.g., Maloney et al. 2005; Scott et al. 2010), as well as Markov Chain Monte Carlo Metropolis-Hastings (MCMCMH) $P(D)$ analyses (e.g., Patanchon et al. 2009; Valiante et al. 2010; Glenn et al. 2010), to be applied to both chopped and unchopped data at many wavelengths. Our implementation of a Monte Carlo simulation $P(D)$ analysis, which is best suited to handle our position-dependent PSF, adopts the methods of Scott et al. (2010).

The basic approach of our $P(D)$ analysis is to parametrize the differential number counts and add a simulated map of sources obeying these number counts (along with their position-

dependent negative sidelobes; see §3.3) to a jackknifed noise map (see §3.2), thereby creating a fully simulated MAMBO sky image. Because of its simple form, our initial parametrization is a single power law with normalization $N_{4\text{mJy}}$ and index δ , such that the differential number counts have the form

$$\frac{dN}{dS} = N_{4\text{mJy}} \left(\frac{4\text{mJy}}{S} \right)^\delta \quad (1)$$

We adopt this form from Laurent et al. (2005), so as to minimize the degeneracy between the normalization and slope of the number counts at the flux density of our typical significant detection ($\simeq 4\text{mJy}$). Next, we optimally filter this fully simulated sky image and compare its PFD to that of the real data using the likelihood (see below) as a goodness-of-fit statistic. We then compute the average likelihood of the data for ten iterations of these model parameters, choose new parameters, and repeat the process. After filling parameter space with likelihood statistics, we identify the best-fit parameters as those giving the maximum likelihood. After the location of this peak in parameter space is identified, we return and sample this one position $\sim 10^3$ times in order to constrain the absolute likelihood value enough to discriminate between fits using different flux density cutoff values (see below).

The likelihood for each sky realization is calculated as follows. Assuming the PFD’s flux bins are uncorrelated, the probability of observing n_i pixels in the i th flux bin given an expectation value of λ_i is given by a Poisson distribution:

$$P(n_i|\lambda_i) = \frac{\lambda_i^{n_i} e^{-\lambda_i}}{n_i!} \quad (2)$$

Therefore, the natural logarithm of the probability $P\{n_i\}$ of observing the full PFD $\{n_i\}$ for a model PFD $\{\lambda_i\}$ (the log-likelihood) is given by

$$\ln P\{n_i\} = \sum_i \ln \left(\frac{\lambda_i^{n_i} e^{-\lambda_i}}{n_i!} \right) = \sum_i n_i \ln \lambda_i - \ln n_i! - \lambda_i \quad (3)$$

We limit the comparison to bins in which $n_i \geq 10$ and use Stirling’s approximation to write the sum as

$$\ln P\{n_i\} \simeq \sum_i n_i - \lambda_i - n_i \ln \left(\frac{n_i}{\lambda_i} \right) \quad (4)$$

In reality our histogram bins are *not* uncorrelated, since our beam solid angle is $\sim 10\times$ larger than the area of one pixel; thus, this expression will serve simply as a comparative metric for choosing a set of best-fitting parameters. The properly calibrated error bars for this estimate can then be found via a Monte Carlo simulation using synthetic images generated from the best-fit model. $P[n_i]$ is therefore a function over the two-dimensional parameter space of $(N_{4\text{ mJy}}, \delta)$, within which the best-fitting model parameters are those that minimize $-\ln P[n_i]$.

We apply the $P(D)$ analysis to the region in the “best” map where the local RMS noise $\sigma \leq 1.25\text{ mJy beam}^{-1}$ before filtering (see Figure 1). This threshold was chosen to maximize the discriminating power of the simulation. If the noise threshold is very low, the region used for analysis has very high sensitivity, but there are fewer pixels available for comparison. If the noise threshold is too high (e.g., we use the full extent of the “best” map), too many regions with differing local noise properties are included, and the signal from the interior of the map is washed out. Our choice of threshold represents a compromise between these two limits, including as many pixels in the analysis as possible while keeping their noise properties as uniform as possible.

Our initial expression of the PFD in terms of 15 bins between -3.5 and $+4.0\text{ mJy beam}^{-1}$, chosen so that all flux bins had ≥ 10 pixels, failed to constrain the model parameters with a unique maximum likelihood. Because the brightest (and most model-constraining) pixels in the histogram are in the sparsely populated bins above 4.0 mJy beam^{-1} , our simulations produced only a best-fit *arc* in parameter space. When we increased the sensitivity to the brightest pixels by adding an additional bin spanning from $4.0 - 5.0\text{ mJy beam}^{-1}$, wide enough to include ≥ 10 pixels, a well-defined global maximum appeared along the previously degenerate arc.

In order to keep the models from diverging at low flux densities, we also imposed a faint-end cutoff in flux density, S_{cut} , which we crudely treated as a third parameter in the $P(D)$ analysis. By stepping through the values $S_{\text{cut}} = 0.3, 0.2, 0.1, 0.05,$ and 0.01 mJy , testing each with a full set of fitting parameters, we found the maximum likelihood values for the power law to be

$41.7 \pm 0.4\%$, $47.7 \pm 0.2\%$, $52.1 \pm 0.2\%$, $53.0 \pm 0.3\%$, and $49.7 \pm 0.5\%$, respectively. The fits improved steadily with decreasing S_{cut} down to 0.05 mJy but then worsened at 0.01 mJy . Thus, the overall best fitting parameters for the power law were $N_{4\text{ mJy}} = 19.7_{-8.8}^{+4.1}\text{ deg}^{-2}\text{ mJy}^{-1}$, $\delta = 3.14_{-0.18}^{+0.14}$, and $S_{\text{cut}} = 0.05\text{ mJy}$ (we quote marginalized 68% double-sided error bars).

Our second number counts parametrization was a Schechter (1976) function of the form

$$\frac{dN}{dS} = N'_{4\text{ mJy}} \left(\frac{4\text{ mJy}}{S} \right)^{\delta'} \exp \left(-\frac{S - 4\text{ mJy}}{S'_{\text{exp}}} \right) \quad (5)$$

Because the full four-dimensional parameter space of the Schechter function $(N'_{4\text{ mJy}}, \delta', S'_{\text{exp}}, S_{\text{cut}})$ is too large to probe with a blind grid-searching routine, we began by fixing S'_{cut} equal to the solution for the power-law model (0.05 mJy). We then alternated the $P(D)$ analysis between varying the parameters $(N'_{4\text{ mJy}}, S'_{\text{exp}})$ and $(N'_{4\text{ mJy}}, \delta')$ until the solutions converged on the same values for all three parameters (convergence was achieved after three iterations). The initial seed guess for S'_{exp} was motivated by naively scaling the $P(D)$ solution at 1.1 mm , found by Scott et al. (2010) using AzTEC data in the GOODS-S field ($S'_{\text{exp}, 1.1\text{ mm}} = 1.30\text{ mJy}$), to 1.2 mm (see §7.1). The results converged to the exponential scaling flux density of $S'_{\text{exp}} = 1.05\text{ mJy}$, which was then held fixed while we proceeded to make full searches over the parameters $(N'_{4\text{ mJy}}, \delta')$ while varying S'_{cut} .

The quality-of-fit for the Schechter function was also greatest for a flux density cutoff of $S'_{\text{cut}} = 0.05\text{ mJy}$. The maximum likelihood values for $S'_{\text{cut}} = 0.2, 0.1, 0.05,$ and 0.01 mJy were $23.8 \pm 0.1\%$, $26.9 \pm 0.1\%$, $28.3 \pm 0.2\%$, and $26.7 \pm 0.4\%$, respectively. The final set of best-fitting parameters for the Schechter function were $N'_{4\text{ mJy}} = 14.5_{-2.7}^{+7.1}\text{ deg}^{-2}\text{ mJy}^{-1}$, $\delta' = 1.86_{-0.23}^{+0.20}$, $S'_{\text{exp}} = 1.05\text{ mJy}$, and $S'_{\text{cut}} = 0.05\text{ mJy}$.

Figure 6 shows full 68% and 95% confidence regions around the parameters of maximum likelihood for both the power law and Schechter function parametrizations. The uncertainty contours were generated via Monte Carlo sampling (used, e.g., in Scott et al. 2010) by taking the best-fit model parameters and using them to generate additional simulated sky realizations. A $P(D)$ analysis was then carried out on each of these realiza-

tions to recover a set of new (scattered) best-fit model parameters. This process was performed ~ 100 times with the same model inputs in order to generate a likelihood density map around the best-fit model parameters.

As an additional constraint on our model fitting and a means of choosing between parametrizations, we also require that the number counts model obey the constraint of the 1.2 mm CIB (see §7.5), which is shown as the shaded region in Figure 6. It is evident in Figure 6 that although the power law parametrization can fit our observations well, it significantly overpredicts the 1.2 mm CIB. In contrast, the Schechter function parametrization is in excellent agreement with the constraint of the CIB. We therefore adopt the Schechter function parametrization as our fiducial model (e.g., Figure 5) for the remainder of the paper. At the highest flux densities the Schechter function and power-law models nominally predict very different behavior; however, our fluctuation analysis is not sensitive to the number counts at flux densities higher than those of our brightest detected sources.

The fact that both the power-law and Schechter function models of the differential number counts fit best when $S_{\text{cut}} = 0.05$ mJy suggests that the 1.2 mm number counts do not keep rising far beyond 0.05 mJy; formally, they may begin to fall between 0.05 and 0.01 mJy, or may already be decreasing by 0.05 mJy. The former case is in agreement with recent surveys of lensing clusters (e.g., Knudsen et al. 2008) that show SMG number counts increase at least as far down as $\simeq 0.1$ mJy at $850 \mu\text{m}$. At 1.2 mm, this corresponds to $S_{1.2 \text{ mm}} \simeq 0.03 - 0.04$ mJy using the submillimeter spectral indices determined from matching detections at $850 \mu\text{m}$, 1.1 mm, and 1.2 mm in the GOODS-N and COSMOS fields (Greve et al. 2008; Chapin et al. 2009; Austermann et al. 2010; see §7.1) This result is in contrast to the analysis of Scott et al. (2010), who found that the choice of S_{cut} did not affect their results. The discrepancy may be due to the fact that their lower resolution ($28''$ HPBW) reduces the effective depth that can be reached before sources begin crowding in the beam, thereby reducing the sensitivity of the $P(D)$ technique.

5. Analysis of bright sources

5.1. Source extraction

We extracted sources from our “best” and “full” maps in a three-step process. First, we minimized the chi-square statistic for a two-dimensional Gaussian profile with an $11''$ FWHM fit at each pixel center. This minimization was achieved quickly by using a matched filter convolution (see, e.g., Serjeant et al. 2003). Given a signal image S_{ij} , an image of the local RMS noise σ_{ij} , and a smaller array describing the telescope’s PSF P_{xy} , the chi-square statistic for a source with flux F located at pixel (i, j) can be written

$$\chi^2(F|i, j) = \sum_{xy} \left(\frac{S_{i-x, j-y} - FP_{xy}}{\sigma_{i-x, j-y}} \right)^2 \quad (6)$$

We ignored the position-dependent negative side-lobes when we applied the matched filter and used only the central Gaussian profile, since the negative residual flux reaches only $\leq 5\%$ of the peak positive intensity (see Figure 4) in the map interior. Additionally, our significant detections are on average farther away from each other than the largest chop throw used during the observations ($48''$), so their effect on our flux measurements will be less than 5% of our strongest sources’ flux densities (i.e., $\lesssim 0.25$ mJy).

By finding the minimum of $\chi^2(F|i, j)$ as a function of F and determining the associated uncertainty ΔF (Serjeant et al. 2003), we obtained

$$\frac{d\chi^2}{dF} = 0 \longrightarrow \frac{F}{\Delta F} = \frac{\sum_{xy} S_{i-x, j-y} W_{i-x, j-y} P_{xy}}{\sqrt{\sum_{xy} W_{i-x, j-y} P_{xy}^2}} \quad (7)$$

as the S/N of each pixel, in terms of the weight map W defined in §3.1. Next, we located the centroid of each source to sub-pixel precision by fitting the PSF to the region in the original signal map at the location of each significant peak in the S/N map, allowing the position of the Gaussian to vary. Figure 7 shows the uncertainty in this best-fit centroid position, derived via Monte Carlo simulations. For the typical flux densities of our significant detections, the average offset between injected and recovered centroids is $1'' - 3''$. Finally, we computed the best-fit flux density by taking the matched-filter weighted average of the flux map, this time with the PSF kernel shifted

by interpolation to the more precise location of the source centroid. After the flux density of each source was recorded, the source was removed from the map by subtracting the flux-scaled PSF from the source location before we searched for the next most significant detection.

By propagating the uncertainty in the signal image through the χ^2 -minimization process, Serjeant et al. (2003) have shown that the uncertainty in the resulting best-fit flux density at position (i, j) is

$$\Delta F(i, j) = \frac{1}{\sqrt{\sum_{xy} W_{i-x, j-y} P_{xy}^2}} \quad (8)$$

We find that this expression consistently *underestimates* the uncertainty in our map. The reason is simply that the derivation by Serjeant et al. (2003) implicitly assumes that the Gaussian noise in the flux image is spatially uncorrelated. In our images, the noise is correlated on a length exactly matching the FWHM of the telescope PSF, and pure noise fluctuations can be amplified along with the real point sources. In order to correct for this underestimate we (1) produce an optimally filtered image and weight map, (2) use this filtered image and weight map to make a S/N ratio map, and (3) rescale the filtered weight map such that the standard deviation of the S/N map equals unity. This empirical calibration corrects for the effects of correlated noise and produces a map with accurate post-filtered flux density uncertainties. The accuracy of the method is evidenced by its matching the *predicted* number of positive excursions in a correlated Gaussian field as a function of S/N level (see §5.4).

The quoted 1σ errors (see columns S_{ν}^{Best} and S_{ν}^{Full} in Table 2) for each detection correspond to the rescaled version of ΔF evaluated using the shuffled noise map at the location of the source (see §3.2). This noise map describes the Gaussian noise of the observations more faithfully than the original signal map, which overestimates the noise by $\sim 5\%$ due to the positive and negative sidelobes from bright sources. Because our noise is well above the estimated confusion limit (§5.3), Gaussian random fluctuations are the dominant source of uncertainty in our measurements.

5.2. Comparison of results for best and full maps

As discussed in §2, control software problems during our first two semesters of observations undermined our confidence in the reliability of the resulting maps. To assess whether the “full” map could be trusted for bright source extraction, we performed two comparisons between our “full” data and observations with pristine calibration. For the first comparison, we carried out the source extraction steps described in Section 5.1 for *both* the “best” and the “full” datasets and compared the properties of the sources recovered from each. Specifically, we began by choosing the eight sources with $S/N \geq 4.5\sigma$ detections in our “best” map: above this threshold, we expect to see fewer than one spurious detection (§5.4). All eight of these sources are recovered with $\geq 5.0\sigma$ significance in the “full” map. Figure 8 shows the locations of these sources in the field, and the locations of the additional $\geq 5.0\sigma$ detections in the “full” map. Each of the eight sources increases in significance between the “best” and the “full” maps. Additionally, all but one of the “full” map’s $17 \geq 5.0\sigma$ sources are identified in the “best” data at lower significance. One source kept the same significance because it lies in the northeast corner of the field, where observations in the first two semesters contribute little additional sensitivity. Further, for these 17 sources, the ratio of the flux densities in the “best” and “full” maps is consistent with unity (Figure 9).

Next, we compared our “full” map to MAMBO on-off photometry by Fiolet et al. (2009) of *Spitzer*-selected high-redshift starburst candidates in the LHN. We tabulated the map flux densities at the positions of the 13 galaxies in their sample that lie within our map’s footprint (two of these turn up as significant detections in our “full” map; we use these sources’ non-deboosted flux densities here) and compared them to the flux densities reported by Fiolet et al. (2009). We found that the flux densities from the two significant detections as well as those from 10 of the 11 non-detections are consistent to within 1σ (see Figure 10; one source is only consistent to within $\sim 1.5\sigma$).

These two successful consistency checks lead us to conclude that the errors in our first two semesters’ data are not at a level that compro-

mises point source detection, at least for high-significance sources. We have therefore proceeded to define our source catalog on the basis of the “full” map. Since the fluctuation analysis described in §4 relies on the authentic reproduction of the field’s noise properties and low-S/N fluctuations, we have restricted this analysis to the “best” data only.

5.3. Confusion

Random Gaussian noise is the uncertainty in the total flux density inside any single *beam* on the sky due to random fluctuations, while confusion noise is an additional uncertainty in the flux density of a single *source* due to the contributions of faint sources within that beam. The “confusion limit” is defined as the flux density threshold at which confusion noise significantly affects the measured flux density of a source, and is commonly taken to be the flux density above which the integrated number counts of all brighter sources reach $\simeq 0.033$ per beam (Condon 1974). In our map, this rule gives $\simeq 0.9$ mJy using $\theta_B = 15.6''$ (in the smoothed \leftrightarrow filtered version of our “full” map) and assuming our best-fit number counts (§4).

We have also made a direct estimate of the confusion noise by comparing the noise in the central regions of the filtered “best” map to the same region in a series of filtered jackknifed noise maps. Since the jackknifed noise maps remove confused as well as bright sources, the increase in average RMS noise in this relatively uniform region indicates our map contains confusion noise at the level of $\sigma_C \simeq 0.24$ mJy beam $^{-1}$. As a consistency check, we have also estimated the confusion noise by generating simulated maps with source populations following our best-fit number counts from 0.05 mJy up to the confusion limit of 0.9 mJy. Due to the central limit theorem, these faint and confused maps with zero mean have roughly Gaussian PFDs and provide approximations of the confusion noise, assuming our model of the number counts. The standard deviation in these maps is 0.21 mJy beam $^{-1}$, in agreement with the measured confusion noise within the uncertainties of the number counts model. We therefore adopt the measured value of $\sigma_C \simeq 0.24$ mJy as our estimate of the confusion noise. The average uncertainty in the flux density of a source in our catalog is 0.62 mJy, indicating that confusion does not dom-

inate our noise budget.

5.4. Spurious sources

We estimated the number of spurious detections as a function of S/N by running our source extraction algorithm on various noise maps (see §3.2). We tested jackknifed noise maps, shuffled noise maps, and simple Gaussian random numbers. The Gaussian random numbers had a spatially varying standard deviation matched to the weight map of the observations. Figure 11 shows the mean total numbers of spurious detections found in 10^3 jackknifed and Gaussian number noise maps, and in 10^2 shuffled noise maps, as a function of S/N. All three styles of noise map are consistent with each other in their ability to produce spurious detections with $S/N \geq 3.0$. This result confirms that for the purposes of extracting high-significance detections, the shuffled noise maps are just as “source-free” as the jackknifed noise maps. Additionally, both are consistent with a Gaussian distribution down to 3.0σ (and likely consistent with Gaussian noise at all S/N, as implied by the PFD histograms in §3). The over-plotted curve in Figure 11 shows the expected number of excursions above a given S/N level in any isotropic and homogeneous Gaussian random field, derived (and thus only formally valid) for high excursions (see, e.g., Chapter 6 of Adler 1981). The agreement at high S/N indicates that our noise maps and source extraction algorithm are well-behaved. For both the “best” and “full” maps, we expect 0.8 (5.4) spurious sources with $S/N \geq 4.5$ (4.0).

A source at high risk of being a spurious detection can be identified by calculating the total probability that the deboosted flux density is ≤ 0 mJy (see, e.g., Austermann et al. 2010; Scott et al. 2010), hereafter referred to as $P(S < 0)$. Using the threshold of $P(S < 0) \geq 0.10$ used by Austermann et al. (2010), we identify only one (ID # 33) high-risk spurious detection in our $S/N > 4.0$ sample (see Table 2).

5.5. Completeness

We estimate the completeness in our data using the Monte Carlo method of searching for injected sources of varying flux density. The inhomogeneous noise in our map means that sources of identical flux density have different probabilities of

being detected in different locations. We account for this effect statistically by performing the completeness simulation assuming sources have equal probability of being located anywhere in the map during the injection process. Although the high-redshift star-forming galaxy population that our observations trace is likely to exhibit clustering, with the brightest galaxy mergers occurring in the most massive dark matter halos (see, e.g., Weiß et al. 2009), the large Δz interval to which millimeter selection is sensitive tends to weaken angular clustering signatures (see however §5.8). We inject model sources with known flux density into our original signal map one at a time at random positions and search for them using the same source extraction algorithm used to create our source list. If an artificial source is recovered with $S/N \geq 4.0$ within $11''$ of the injected location, it is considered detected. The injection process was repeated 10^3 times for each flux density in a logarithmic grid from 1.0 mJy to 10.0 mJy; the average recovery percentage is shown in Figure 12. Our map is 80% complete at 3.7 mJy and 50% complete at 2.6 mJy. We also tabulated the angular separations between the injected and recovered source positions to characterize the uncertainties in the positions of our actual significant detections (ignoring telescope pointing errors). For $S_{1.2\text{mm}} \gtrsim 2$ mJy, the average position error $\langle \Delta\theta \rangle \leq 3''$ (see Figure 7).

5.6. Flux boosting

To correct the measured flux densities of our detections for the effect of “flux boosting,” we use the Bayesian technique described in Coppin et al. (2005), which because of its versatility in handling both chopped and unchopped data has been adapted for use at many wavelengths (e.g., Coppin et al. 2006; Greve et al. 2008; Scott et al. 2008; Perera et al. 2008; Scott et al. 2010; Austermann et al. 2010). Using Bayes’s Theorem and the prior information of the number counts functional form found from our $P(D)$ analysis (§4), the probability that a source has true flux density S_0 given a measurement S with uncertainty σ is equal to

$$P(S_0|S, \sigma) = \frac{P(S, \sigma|S_0)P(S_0)}{P(S, \sigma)} \quad (9)$$

where $P(S, \sigma|S_0)$ is the posterior probability, $P(S_0)$ is the prior flux density distribution,

$P(S, \sigma|S_0)$ is the likelihood, and $P(S, \sigma)$ is the prior measurement distribution. $P(S, \sigma)$ is independent of S_0 , so only acts to normalize the expression such that $\int P(S_0|S, \sigma)dS_0 = 1$; hereafter, it will be ignored. We have shown that the uncertainty in our map is dominated by Gaussian random noise, so $P(S, \sigma|S_0)$ takes the form

$$P(S, \sigma|S_0) \propto \exp \left[-\frac{(S - S_0)^2}{2\sigma^2} \right] \quad (10)$$

To estimate the prior flux distribution in the map ($P(S_0)$), we assembled a PFD containing the pixels from 10^4 noise-free random sky realizations that used the best-fit number count parameters from our $P(D)$ analysis. The peak value and 68% double-sided confidence intervals of the resulting posterior probability function ($P(S_0|S, \sigma)$) were found numerically for each measured flux density and uncertainty. Figure 13 shows four examples of the deboosting process, each in a different regime of source S/N. If the S/N is too low, and the integration of the confidence intervals does not converge, we instead use an analytic formula to estimate the deboosted flux density. For this, we generalize the formalism of Hogg & Turner (1998) to a Schechter function, and locate the maximum of the posterior flux distribution:

$$P(S_0|S, \sigma) \propto S_0^{-\delta'} \exp \left[-\frac{S_0}{S'_{\text{exp}}} - \frac{(S - S_0)^2}{2\sigma^2} \right] \quad (11)$$

where δ' and S'_{exp} are the power-law slope and exponential scale factor of the Schechter function, respectively. By solving for S_0 when the derivative of the above expression vanishes, we find the highest posterior probability to be achieved for

$$S_{\text{true}} = \frac{S S'_{\text{exp}} - \sigma^2 + \sqrt{(\sigma^2 - S S'_{\text{exp}})^2 - 4 \delta' S'_{\text{exp}} \sigma^2}}{2S'_{\text{exp}}} \quad (12)$$

To ensure that our adaption of the Bayesian method of flux deboosting returns a properly corrected estimate of the true number counts, we performed a Monte Carlo simulation to directly calculate the observed number counts of random sky realizations populated with source distributions following our best-fit number counts (see,

e.g., Coppin et al. 2006). Figure 14 shows the results of this consistency check. This simulation demonstrates that the Bayesian method of flux deboosting performs well in recovering the original injected number counts. The residual scatter of the average recovered number counts around the average input model in Figure 14 demonstrates the level of systematic error in the algorithm, which is significantly smaller than the statistical error of our differential number counts estimate (see Figure 15).

5.7. Direct calculation of number counts

While our catalog of detections includes all sources with $S/N > 4.0$, we use only detections with $S/N > 4.5$ for our direct calculation of the number counts because above this threshold, we expect to detect less than one spurious source (see Figure 11). Table 3 presents integral and differential number counts after correction for completeness and flux boosting. Figure 15 shows our directly calculated number counts, along with the 95% confidence regions for the best-fit power law and Schechter function models of the differential number counts found from the $P(D)$ analysis. These two independent methods of estimating the number counts are in agreement with each other. This consistency is encouraging because the $P(D)$ analysis and the direct estimate of number counts depend on the faint and bright pixel values in different ways.

5.8. Clustering

The group of sources in the southeast corner of our field, as well as the large void in the center, prompted us to perform a clustering analysis to determine whether or not the distribution of sources in our map is statistically clustered or not. To perform the analysis, we used the Landy & Szalay (1993) correlation function estimator:

$$w(\theta) = \frac{DD - 2DR + RR}{RR} \quad (13)$$

with variance

$$\langle \Delta w(\theta) \rangle^2 \simeq \frac{(1 + w(\theta))^2}{RR} \quad (14)$$

(Gawiser et al. 2006). In the equations above, DD , RR , and DR represent the normalized numbers of unique galaxy-galaxy, random-random,

and galaxy-random pairs with angular separations $\theta \pm d\theta/2$. This estimator is used frequently in extragalactic deep field analyses (e.g., Borys et al. 2003; Scott, Dunlop, & Serjeant 2006; Weiß et al. 2009), and has been shown to have nearly Poisson variance and zero bias (Landy & Szalay 1993). We take into account the geometric boundary of the map and the variation in detectability with position by generating the random locations with the same Monte Carlo algorithm used for the $P(D)$ analysis. We inject ensembles of sources following our best fitting number counts into a noise map at random locations and use the positions of sources detected with $S/N > 4.0$ as our random coordinates. This Monte Carlo technique is important for ensuring that we do not misinterpret depth variation in the map as a clustering signal.

To confirm that this technique is unbiased, we also performed the full clustering analysis on only random positions to check that we recovered a flat $w(\theta) = 0$ response (see Figure 16). For small separations ($\lesssim 2'$), however, it turns out that $w(\theta)$ does not return zero in our data: depending on the position within the map, the negative sidelobes can suppress the flux densities of nearby sources enough to lower their S/N ratios below the detection threshold. This effect begins to have an effect at $\simeq 2\times$ the chop throw (of which the maximum used in any semester was $48''$), and has a strong effect at separations $\leq 1\times$ chop throw. Because this effect suppresses the detection of RR and DD pairs but not DR pairs, the zero-clustering baseline for chopped data like ours is less than zero at these small angles. In order to assess the clustering in the map while taking this bias into account, we measure the effective clustering relative to the zero-clustering baseline for these separations ($\lesssim 2'$).

The result of our Monte Carlo clustering analysis is shown in Figure 16. We find a small clustering signal when using all detections with $S/N > 4.0$ that agrees reasonably well with the angular correlation function measured by Scott, Dunlop, & Serjeant (2006), who combined many different SCUBA $850\ \mu\text{m}$ blank field maps, and that shows stronger clustering (albeit at lower S/N) than the correlation function measured by Weiß et al. (2009) at $870\ \mu\text{m}$ in the ECDF-S. Williams et al. (2011) have analyzed the clustering of $3.0\text{--}3.5\sigma$ $1.1\ \text{mm}$ detections in a $0.72\ \text{deg}^2$

map of the COSMOS field with ASTE/AzTEC, concluding that it is difficult to recover reliable clustering parameters for SMGs from maps whose angular resolution and total area are limited. This result argues for caution in interpreting our clustering analysis, although we do benefit to an extent from MAMBO’s relatively high angular resolution. An interesting feature in our correlation function is the spike near $\theta \simeq 4'$. This signal is due to the rich group of sources in the southeastern corner of the map, all at typical relative spacings of a few arcminutes from each other (see also §7.4). It may be noteworthy that Weiß et al. (2009) find a $\sim 2.4\sigma$ spike above their best fitting model of $\omega(\theta)$ at a scale of $\sim 5'$, near where Williams et al. (2011) also detect a slight positive excess in $\omega(\theta)$. When performing the analysis on only our (27) most significant sources with $S/N > 4.5$, we find no significant clustering signal.

Following the analysis of, e.g., Borys et al. (2003) for the SCUBA “Supermap,” we also use the method of Scott & Tout (1989) to analyze the cumulative distribution of nearest neighbors to test whether our galaxy positions are consistent with being drawn from a random distribution (see Figure 17). Because the nearest neighbor analysis is sensitive to the total number of positions used, we use the 41 most significant detections in *each* Monte Carlo realization, instead of all of those detections with $S/N > 4.0$ as in the correlation function analysis. Because the number counts rise quickly, the S/N of the least significant discovered source varies, but is always close to 4.0. A Kolmogorov-Smirnov test rules out the null hypothesis that our significant detections are drawn from a random position distribution at the 95% confidence level, implying that the source locations in the map (e.g., defining the southeastern clump and the central void) are not arranged randomly.

6. Counterpart identification

We have calculated the corrected probability of chance associations (P ; Downes et al. 1986) between our MAMBO detections and possible counterparts at the other wavelengths at which the LHN has been observed (see Table 2). The P statistic is defined by

$$P = 1 - e^{-E} \quad (15)$$

for $E = P^*[1 + \ln(P_c/P^*)]$, $P^* = \pi r^2 N(> S)$, and $P_c = \pi r_s^2 N_c$, in terms of the brightness of the counterpart S , the source separation r , the search radius r_s , the number density of sources brighter than S $N(> S)$, and the number density of sources at the sensitivity limit N_c . Based on the results of the position error analysis (see Figure 7), we chose a counterpart search radius of $8''$. Because positional uncertainty $\sigma \propto \text{FWHM} \times \text{SNR}^{-1}$, our $11''$ beam is the dominant source of error, and we ignore the positional uncertainties at other wavelengths. We consider $P < 0.01$ to define a robust counterpart, $0.01 \leq P < 0.05$ a likely counterpart, and $P \geq 0.05$ an unlikely association.

6.1. 20 cm counterparts

We used the NRAO VLA Sky Survey (NVSS) and the deep SWIRE number counts of Condon et al. (1998) and Owen & Morrison (2008), respectively, in the calculation of P to assess the significance of 20 cm counterparts. The 20 cm VLA pointing of the LHN has a central RMS sensitivity of $2.7 \mu\text{Jy}$, rising to $\sim 4\text{--}5 \mu\text{Jy}$ near the edges of our MAMBO map. When we compare our 41 $S/N > 4.0$ detections to the 5σ 20 cm catalog of Owen & Morrison (2008), 44% (18) have robust counterparts, and 41% (17) have likely counterparts. We have also reexamined the 20 cm map in the vicinity of the remaining MAMBO sources and have identified one additional robust counterpart (ID # 9), two likely counterparts (ID # 28 and # 36), and one unlikely counterpart (ID # 20) at the $4\text{--}5\sigma$ level. We also deblended one likely counterpart into one robust and one unlikely counterpart (ID # 17). After including these additional sources, 49% (20) of our MAMBO detections have robust counterparts, 44% (18) have likely counterparts, and 7% (3) have unlikely or no detected counterparts. We performed a Monte Carlo simulation to test the reliability of our P values and found that $4.9 \pm 0.2\%$ of randomly chosen positions within our MAMBO field have a likely radio counterpart ($P < 0.05$) within $8''$, confirming the validity of the high number of robust associations. We expect ~ 5 spurious detections above $S/N > 4.0$; thus, the handful of sources with unlikely or no radio counterparts may be spurious

detections if they do not lie at a very high redshift. One MAMBO source (ID # 32) with an unlikely ($P_{20\text{ cm}} = 0.056$) radio counterpart also has a likely ($P_{250\text{ }\mu\text{m}} = 0.016$) *Herschel* counterpart (Magdis et al. 2010), arguing against its being a spurious detection.

6.2. 50 cm radio counterparts

We have extracted 50 cm flux densities from the GMRT map (Owen et al. 2011a) with the same technique used at 20 cm and 50 cm (see Owen & Morrison 2008; Owen et al. 2009b). The uncertainties listed in Table 2 reflect the local RMS noise in the image and do not include a $\sim 3\%$ calibration error or a spatially varying GMRT pointing error. Two of the 50 cm detections are heavily blended with bright neighbors, so for these counterparts we report only tentative fluxes. Of the 40 tabulated 20 cm counterparts (including the two with $P > 0.05$), all 40 have 50 cm counterparts. The one 20 cm non-detection (within $8''$) is also a 50 cm non-detection.

6.3. 90 cm radio counterparts

To search for 90 cm counterparts, we used the 90 cm radio catalog of Owen et al. (2009b), which has an RMS sensitivity of $10\text{ }\mu\text{Jy}$. Of our 41 MAMBO sources, 24% (10) have 90 cm counterparts. Each of the ten 90 cm counterparts is also detected at 50 and 20 cm with $P_{20\text{ cm}} < 0.05$.

6.4. 24 μm counterparts

In addition to SWIRE 24 μm observations of the LHN (3σ depth of $209\text{ }\mu\text{Jy}$), there exist deeper *Spitzer*/MIPS data with a 3σ depth of $18\text{ }\mu\text{Jy}$ (Owen et al. 2011b). We searched for 24 μm counterparts to our MAMBO detections in this deeper MIPS image. To calculate P statistics for 24 μm counterparts, we used the counts of Béthermin et al. (2010). A Monte Carlo simulation of the 24 μm P -statistic finds that $4.7 \pm 0.3\%$ of random positions yield a counterpart with $P < 0.05$. Within our sample of 41 MAMBO sources, 20% (8) have robust 24 μm counterparts, and 29% (12) have likely counterparts.

6.5. X-ray counterparts

Only one source (MM J104522.8+585558 = ID # 26) has a likely X-ray counterpart (CX-

OSW J104523.6+585601; Wilkes et al. 2009). The X-ray source is at a distance of $7.2''$ and has a broad band (0.3–8.0 keV) flux of $(2.5 \pm 1.1) \times 10^{-15}\text{ erg cm}^{-2}\text{ s}^{-1}$ (Polletta et al. 2006). By using the 2.5–7 keV flux of $1.58 \times 10^{-15}\text{ erg cm}^{-2}\text{ s}^{-1}$ together with the *Chandra*/SWIRE counts from 2–8 keV (Wilkes et al. 2009) we can set an upper limit on the probability of chance association of $P \lesssim 0.02$.

7. Discussion

7.1. Number counts vs. previous deep fields

Previous deep surveys at 1.2 mm using MAMBO (e.g., Greve et al. 2004; Bertoldi et al. 2007) have returned directly calculated 1.2 mm number counts in the Lockman Hole East (LHE), ELAIS-N2, and COSMOS fields. The parameters of these surveys are listed in Table 4; we compare their results to our directly calculated counts, as well as to our best-fit $P(D)$ models, in Figure 15. We find that our power-law slope is consistent with their results, but our results have a lower overall normalization. This difference in normalization might be due to the different methods used in the number counts calculations. We have used the Bayesian method of flux deboosting presented in Coppin et al. (2005), and only include our most significant detections in the calculation. The analyses of Greve et al. (2004) and Bertoldi et al. (2007) use the method of injecting sources into noise maps to determine their flux deboosting correction, and include sources with lower S/N in their number counts calculation. In principle, any S/N cutoff would be acceptable for the latter calculation as long as the completeness correction uses the same threshold; however, lower S/N thresholds will lead to more spurious detections. Both of these effects could be contributing to their higher normalization. However, considering the relatively large error bars on all the measurements and the internal variation among the ELAIS-N2, LHE, and COSMOS datasets themselves, the results are still nearly consistent.

Because a single power-law parametrization of the number counts is commonly used to compare the results of deep surveys, we begin by noting that our best-fit power law index ($\delta = 3.14_{-0.18}^{+0.14}$) is consistent with the results of surveys at other

wavelengths that fit their number counts using a similar (single power-law) model. Coppin et al. (2006) find $850\ \mu\text{m}$ power-law indices of $\delta = 2.9 \pm 0.2$ and $\delta = 3.0 \pm 0.3$ in the LHE and Subaru/XMM-Newton deep fields, respectively. Using Bolocam data at $1.1\ \text{mm}$, Laurent et al. (2005) estimate a power-law index of $\delta = 3.16$ from directly calculated counts in the Lockman Hole. However, Maloney et al. (2005) performed a $P(D)$ analysis on the same $1.1\ \text{mm}$ Bolocam data and find $\delta = 2.7^{+0.18}_{-0.15}$. Although it is well within the $1\ \sigma$ uncertainties of the Laurent et al. (2005) result, the latter slope differs from ours by $> 2\sigma$. In this case, differences in the methods of our $P(D)$ analyses might be the differentiating factor. Maloney et al. (2005) also used chopped observations in their analysis, for example, but ignored the effects of chopping on the PFD. It is possible that by not including the negative residual flux in their $P(D)$ analysis, they required many fewer faint sources to match the pixel distribution of the real data (and therefore derived a shallower power law slope). However, a value of $\delta \simeq 2.7$ is also the best-fit single power-law slope found by Scott et al. (2010) for their $P(D)$ analysis of unchopped $1.1\ \text{mm}$ AzTEC data in the GOODS-S field.

In Figure 15 (see also Table 4), we also compare our results to those for deep field observations at $1.1\ \text{mm}$ by AzTEC of the COSMOS (Scott et al. 2008), GOODS-N (Perera et al. 2008), GOODS-S (Scott et al. 2010), SHADES (Austermann et al. 2010), and AKARI, SSA-N2, and SXDF (Hatsukade et al. 2011) deep fields. (For clarity, the observations of Hatsukade et al. (2011) and Perera et al. (2008) are not shown in the plot because their data points lie within the scatter of the other AzTEC observations.) We also compare our results to the extremely deep SMG counts measured in lensing fields at $850\ \mu\text{m}$ by Knudsen et al. (2008) as well as the recent wide map by Weiß et al. (2009) using LABOCA at $870\ \mu\text{m}$ in the ECDF-S. In order to compare our number counts directly to the results of these surveys at other wavelengths, we rescale their flux densities. Our choice of rescaling factor is based on the direct comparisons between $S_{850\ \mu\text{m}}$, $S_{1.1\ \text{mm}}$, and $S_{1.2\ \text{mm}}$ for galaxies in the GOODS-N field. The average flux density ratio for sources with robust SCUBA and AzTEC detections in

the GOODS-N field is $S_{850\ \mu\text{m}}/S_{1.1\ \text{mm}} \simeq 1.8 - 2.0$ (Perera et al. 2008; Chapin et al. 2009). When comparing SCUBA and MAMBO detections, Greve et al. (2008) find $S_{850\ \mu\text{m}}/S_{1.2\ \text{mm}} \simeq 2.5$. By coadding the MAMBO and AzTEC observations in the GOODS-N field into a map at an effective wavelength of $\lambda = 1.16\ \text{mm}$, Penner et al. (2011) find an average value of $S_{1.16\ \text{mm}}/S_{1.1\ \text{mm}} \sim 0.88$ and $S_{1.16\ \text{mm}}/S_{1.2\ \text{mm}} \sim 1.14$. All of these results are consistent with a single modified blackbody spectrum, for $\beta = 1.5$ and $T_d = 30\ \text{K}$, observed at $z \simeq 2.5$. Therefore, we adopt this fiducial galaxy model when comparing fluxes at different wavelengths and use $S_{850\ \mu\text{m}}/S_{1.2\ \text{mm}} = 2.3$, $S_{870\ \mu\text{m}}/S_{1.2\ \text{mm}} = 2.2$, and $S_{1.1\ \text{mm}}/S_{1.2\ \text{mm}} = 1.2$. Our directly calculated counts are in excellent agreement with the rescaled results of the AzTEC surveys. Additionally, our prediction for the shape of the number counts below our sensitivity threshold, afforded by our $P(D)$ analysis, agrees well with the deepest AzTEC number counts and is even in rough agreement with the deepest SMG counts by Knudsen et al. (2008).

Figure 15 also compares our results to various number count predictions derived from backward evolution models that incorporate multi-wavelength observations of number counts and redshift distributions, as well as limits imposed by the CIB light. We have restricted this comparison to models that offer predictions at wavelengths of $1.2\ \text{mm}$ (Béthermin et al. 2011) or at $1.1\ \text{mm}$ (Valiante et al. 2009; Rowan-Robinson 2009; Marsden et al. 2011), to which we can apply the rescaling described above. Although flux scaling will generally not provide a precise representation of a model's predictions at $1.2\ \text{mm}$, the extrapolation from $1.1\ \text{mm}$ to $1.2\ \text{mm}$ is fairly modest. At flux densities equal to or less than those of our significant detections, we find that our observations are generally consistent with all model predictions, although the Valiante et al. (2009) model slightly overpredicts our $P(D)$ curve near $1\ \text{mJy}$. At the high flux density limit, all models uniformly overpredict the counts from our best-fitting Schechter function model, while remaining consistent with the predictions from our power-law result (which is only marginally compatible with the CIB; see Figure 5). However, we cannot draw any conclusions from this apparent discrepancy, as our $P(D)$ analysis cannot constrain the

differential counts at flux densities greater than those of our brightest detections.

7.2. Fractional counterpart identification

Here we investigate the question of whether our radio counterpart identification rate ($R_{1.4\text{ GHz}}$) of $\simeq 93_{-7}^{+4}\%$ (38/41) in the LHN is intrinsically greater than is seen in other surveys, or if it is simply a function of the increased 20 cm sensitivity in this field. We compare our identification rate to those found for previous deep surveys at $850\ \mu\text{m}$, $870\ \mu\text{m}$, $1.1\ \text{mm}$, and $1.2\ \text{mm}$. Table 5 lists recent millimeter and submillimeter deep field surveys from the GOODS-N, LHE, SXDF, COSMOS, and ECDFS fields (Borys et al. 2003, 2004; Ivison et al. 2007; Bertoldi et al. 2007; Schinnerer et al. 2007; Perera et al. 2008; Chapin et al. 2009; Weiß et al. 2009; Biggs et al. 2011), along with their 20 cm radio counterpart identification rates and 20 cm map sensitivities. Because the surveys have different definitions of “significant” (sub)millimeter detections, different data reduction techniques, and different standards for radio counterpart associations, we marginalize over all of these variables by looking at the average radio counterpart identification rate, and the average 20 cm map sensitivity. Using the surveys listed in Table 5, we find $\langle\sigma_{1.4\text{ GHz}}\rangle \simeq 7.2\ \mu\text{Jy}$ and $\langle R_{1.4\text{ GHz}}\rangle \simeq 57\%$.

If we imagine that our field had a sensitivity $\langle\sigma_{1.4\text{ GHz}}\rangle \simeq 7.2\ \mu\text{Jy}$, six of our likely radio counterparts would fall below the 4.0σ limit of $S_{1.4\text{ GHz}} < 29\ \mu\text{Jy}$ and would not be detected. Four additional likely 20 cm counterparts would appear at the $4\text{--}5\sigma$ level and would be at high risk of not being detected due to the usual completeness effects. Therefore, our radio counterpart identification rate would be $68_{-9}^{+8}\%$ – $78_{-8}^{+7}\%$. This range is only marginally greater than the average value of 57%, and well within the scatter of the previous surveys. Therefore, we attribute our high radio identification rate to the extremely sensitive VLA map of this field, rather than to unusual properties of 1.2 mm-selected sources at this depth.

Because we expect ~ 5 spurious detections among our 41 sources with $S/N > 4.0$ and we find only 2–3 detections with unlikely or no radio counterparts, there is little room left to accommodate a substantial, extremely high-redshift

($z > 5$) population of radio-undetected SMGs (see also Ivison et al. 2005). This work suggests that with a deep enough radio image, perhaps all SMGs might have their radio counterparts identified, auguring well for upcoming deep surveys that exploit the dramatically expanded correlator bandwidth of the EVLA.

We find that $7.3_{-4.0}^{+6.7}\%$ (3/41) of our detections have two likely radio counterparts (MAMBO ID # 3, 15, and 39). If we consider the fact that 5% of all randomly chosen positions within our MAMBO map will have counterparts within $8''$ with $P \leq 0.05$, then we would expect to find a double radio counterpart rate of $\sim 4.6\%$ from chance associations. Previous studies have found that $\sim 10\%$ of SMGs host multiple likely radio counterparts (see, e.g., Ivison et al. 2002, 2007; Pope et al. 2006), probably due to the effects of confusion within the submm/mm image, physical interactions, or the extended jets of radio-loud AGN. Although our SMG sample in the LHN is too small to be able to constrain the fraction of multiple radio counterparts to better than $\pm 5\%$, we note that the pair separations of the radio counterparts are $2.1''$, $7.7''$, and $7.4''$, and that two of the three MAMBO sources have deboosted flux densities in the top 25% of our sample. These results may be in agreement with the trend identified in Ivison et al. (2007) that multiple radio counterparts are preferentially associated with the brightest SMGs, and have pair angular separations $\Delta\theta \simeq 2''\text{--}6''$.

7.3. Redshift distribution

As listed in Table 2 and detailed in Appendix A, of our 41 significant individual detections, two have optical spectroscopic redshifts (Polletta et al. 2006; Owen & Morrison 2009a), two have mid-IR spectroscopic redshifts (Fiolet et al. 2010), and two have high-quality photometric redshifts based on *Herschel* far-IR photometry that we will denote in what follows as “ z'_{phot} ” (Magdis et al. 2010). For those of the remaining 35 sources with robust or likely radio counterparts, we generally adopt the optical photometric redshifts (denoted z_{phot} in what follows) determined by Strazzullo et al. (2010) for the radio catalog of Owen & Morrison (2008). The exception to this rule comes for $\{z_{\text{phot}}\}$ to which Strazzullo et al. (2010) assign a goodness-of-fit quality flag of “C”; these redshifts

are less reliable, and in particular are more likely to manifest catastrophic errors. For such sources, as well as for the one 1.2 mm detection that lacks a radio counterpart altogether, we instead derive our own redshift estimates (z_α) using the radio-submillimeter spectral index redshift indicator of Carilli & Yun (1999):

$$\alpha_{1.4}^{350} = -0.24 - [0.42 \times (\alpha_{\text{radio}} - \alpha_{\text{submm}}) \times \log_{10}(1 + z_\alpha)] \quad (16)$$

(see also Carilli & Yun 2000; Yun & Carilli 2002).

For α_{radio} we use, in order of priority and availability, $\alpha_{20\text{cm}}^{90\text{cm}}$, $\alpha_{20\text{cm}}^{50\text{cm}}$, or -0.68 . We use $\alpha_{20\text{cm}}^{50\text{cm}}$ only for sources with clean, unblended 50 cm detections. For these unblended 50 cm counterparts, we find an average value of $\langle \alpha_{20\text{cm}}^{50\text{cm}} \rangle = -0.68 \pm 0.06$ (see Figure 18), in agreement with the average spectral index of SMGs in the LHE field of $\langle \alpha_{20\text{cm}}^{50\text{cm}} \rangle = -0.75 \pm 0.06$ (Ibar et al. 2009, 2010). We adopt this mean value of $\alpha_{20\text{cm}}^{50\text{cm}}$ (-0.68) for redshift determination of sources with *only* 20 cm radio counterparts, or whose 50 cm counterparts are confused. For α_{submm} , we use the spectral index at 1.2 mm of the fiducial high-redshift dusty galaxy SED ($\alpha_{\text{submm}} = 3.2$), as motivated in §7.1. For our detection with no likely radio counterpart, we estimate a redshift lower bound by using the local $S_{20\text{cm}} 4\sigma$ upper limit in Equation 16.

Figure 19 illustrates why we exclude C-quality photometric redshifts from our catalog. Plotted is the $\alpha_{1.4}^{350}$ spectral index of the detections as a function of z_{phot} . The points are coded according to photometric redshift quality flag (Strazzullo et al. 2010). The points with the best photometric redshift fit quality (AA) are shown as black circles, followed by blue squares (A), green diamonds (B), and red triangles (C). The shaded region shows the Carilli & Yun (1999) relation for $-\alpha_{\text{radio}} = 0.52 - 0.80$, where -0.52 represents the median $\alpha_{20\text{cm}}^{90\text{cm}}$ spectral index in the LHN field (Owen et al. 2009b) and -0.80 is the fiducial synchrotron value (Condon 1992). The over-plotted lines show the empirical relations recovered by redshifting the SEDs of nearby star-forming galaxies M82 and Arp 220 (Klein et al. 1988; Scoville et al. 1991). The highest quality photometric redshifts agree with their galaxies' spectral indices in that they either follow the Carilli & Yun relation, or are consistent with an M82 or Arp 220 SED. In contrast, the C-quality photometric redshifts are scattered almost uniformly in z for a given $\alpha_{1.4}^{350}$, demon-

strating their lack of robustness.

Figure 20 shows the redshift distribution of our catalog, including all spectroscopic, photometric, and $\alpha_{1.4}^{350}$ -estimated redshifts. It is apparent in Figure 20 that the 17 spectroscopic and high-quality (*Herschel* and AA/A/B-grade optical) photometric redshifts are biased towards lower redshifts. The median redshift for this 41% of our sample is $z_{\text{median}} = 2.26$, with an inter-quartile range of 1.72–2.90. For all galaxies, $z_{\text{median}} = 2.90$, with an inter-quartile range of 2.33–3.70. This systematic bias has two causes. First, the highest-redshift galaxies have the faintest counterparts, and will necessarily be detected in fewer optical bands, which results in a poorer fit. This trend is in contrast to the full radio catalog, for which the median z_{phot} is ~ 1 and the fraction of photometric redshifts with AA/A/B quality ($\sim 85\%$) is much higher than for our MAMBO sources. Second, the SEDs in the Strazzullo et al. (2010) galaxy template library are most representative of nearby galaxies, potentially resulting in a poor fit if they are applied to high- z galaxies whose SEDs are not included in that library.

The median redshift for our sample ($z_{\text{median}} = 2.90$) is larger than the median redshift determined by Pope et al. (2006) for a complete sample of 850 μm -selected SMGs with spectroscopic redshifts ($z_{\text{median}} = 2.0$). Although our redshift distribution has greater uncertainties because it relies heavily on photometric redshifts and spectral index redshift estimates, it is in agreement with the results of Chapin et al. (2009), who have shown that, with high statistical significance, galaxies in a sample selected at 1.1 mm are detected at higher redshift ($z_{\text{median}} = 2.7$) than those selected at 850 μm . Our median redshift is also greater than that of the sample of 68 galaxies selected at 870 μm from the LABOCA survey of the ECDF-S. Using 17-band optical through mid-IR photometry, Wardlow et al. (2011) find $z_{\text{median}} = 2.2$.

7.4. Spatial correlation with 20 cm sources

The results from the $w(\theta)$ and nearest neighbor analyses (§5.8) suggest that our sources are clustered to some degree. The spike in $w(\theta)$ on $\sim 4'$ scales is an intriguing result that is consistent with the visual impression of Figure 2 (i.e., the southeastern overdensity and the central void) and hints at the existence of large-scale structure

(LSS) in this field. To investigate whether the spatial distribution of our detections traces LSS that can also be seen at other wavelengths, we compare our source positions to the distribution of radio sources within the LHN. In order to compare our MAMBO sources to radio sources at comparable redshifts, we include only radio sources with $1.5 < z_{\text{phot}} < 4.5$ (excluding all that only have a C-quality z_{phot}). Additionally, we only consider radio sources with sizes greater than $1.0''$. These larger sources will be preferentially gas-rich mergers with extended star formation or radio-loud AGN, which we would naively expect to trace environmental overdensities on the basis of studies at lower redshift (e.g., Hill & Lilly 1991; Best 2004; Best et al. 2005; Wake et al. 2008). From a practical standpoint, they can also be detected over the full area of the MAMBO map, allowing for a fair comparison; sources with 20 cm sizes $\leq 1''$, in contrast, tend to be fainter, and therefore have systematically lower surface densities farther from the center of the VLA map.

In Figure 21, we plot our 1.2 mm source positions over a $3'$ -resolution smoothed surface density map of the 307 radio sources in the Owen & Morrison (2008) VLA catalog that satisfy our selection cuts. We find that the distributions of the two populations agree quite well: (1) the density map shows a deficiency of radio sources at the location of our central MAMBO void, (2) every radio source density peak ($\langle \Sigma_{20 \text{ cm}} \rangle \geq 0.5 \text{ arcmin}^{-2}$) is associated with at least one MAMBO detection, and (3) $\sim 66\%$ of our MAMBO detections are located in regions with higher than average ($\langle \Sigma_{20 \text{ cm}} \rangle \geq 0.34 \text{ arcmin}^{-2}$) radio source density, whose area comprises only 45% of the total. This striking agreement seems to argue for a real physical correlation between our MAMBO detections and 20 cm radio galaxies at similar redshifts. Following Austermann et al. (2009), we have also compared our SMG catalog to an identical number of homogeneously distributed, randomly chosen positions. The experiment confirms the spatial correlation at a confidence level of 90%. However, when using random positions derived from our simulated maps that take into account the spatially varying sensitivity, we find that our MAMBO detections, although significantly correlated with each other, are not significantly spatially correlated with this

sample of high- z 20 cm galaxies.

7.5. Resolving the 1.2 mm CIB

At 1.2 mm, the cosmic infrared background (CIB) intensity is $I_\nu \simeq 15\text{--}24 \text{ Jy deg}^{-2}$ (Puget et al. 1996; Fixsen et al. 1998). By adding up the deboosted flux densities of our detections with $S/N > 4.0$, we recover $\simeq 0.58 \text{ Jy deg}^{-2}$ of the CIB, or about $\sim 3\%$. Figure 5 shows that our best fitting Schechter function estimate of the differential number counts is entirely consistent with the intensity of the CIB, while the power-law model is only marginally compatible with it. The analysis performed by Scott et al. (2010) on ASTE/AzTEC data in the GOODS-S field finds that the best-fit power law model from their $P(D)$ analysis can account for the CIB, although only if they integrate the counts past the cutoff used for that analysis. They also find that their Schechter function model is incompatible with the CIB, and can only recover $\sim 30\%$ of the 1.1 mm background when integrated down to $S'_{1.1 \text{ mm}} = 0 \text{ mJy}$. These results may be due to their a priori choice of a faint-end power-law index $\delta' = 1.0$. We fit for this parameter directly and find that a steeper value of $\delta' \simeq 1.86$ is optimal for our data and produces enough faint sources to account fully for the CIB light at 1.2 mm.

8. Conclusions

We have presented a 566 arcmin^2 map of the Lockman Hole North field with an average optimally filtered point source sensitivity $\simeq 0.75 \text{ mJy beam}^{-1}$. By making use of previously developed and original techniques to handle chopped bolometer array data, along with $P(D)$ -based number counts and clustering analyses, we have assembled a comprehensive picture of the 1.2 mm sky. Our results provide valuable new constraints for models of the evolution of dusty starburst galaxies through cosmic time.

We detect 41 1.2 mm sources at $S/N > 4.0$ in our final map. Of these 41 detections, 38 have robust or likely ($P < 0.05$) 20 cm radio counterparts, and 20 have robust or likely counterparts at $24 \mu\text{m}$. Based on Monte-Carlo simulations, we expect ~ 5 of these detections to be spurious, and only ~ 2 20 cm counterparts with $P < 0.05$ to be chance associations. This result gives our MAMBO/LHN

map the highest single-field SMG radio counterpart identification rate ever observed ($93_{-7}^{+4}\%$), which we have shown can be explained entirely by the extraordinary depth of our 20 cm VLA map. The enhanced sensitivity of the EVLA will be able to make high counterpart fractions routine for future SMG samples. Based on the spectroscopic, photometric, and radio/far-infrared spectral index redshifts of these counterparts, the median redshift of our sample is $z_{\text{median}} = 2.9$, higher than has been determined for 850 μm -selected SMG samples in fields with shallower VLA coverage.

We estimate the number counts of 1.2 mm sources both directly and by using a $P(D)$ analysis and find a similar slope but a lower overall normalization relative to previous MAMBO surveys. However, our results are in close agreement, after a scaling in flux density, with those of recent surveys at 1.1 mm. The compatibility of our directly calculated counts and $P(D)$ analysis with the constraint of the 1.2 mm CIB demonstrate the robustness of our results. In particular, we find that for $S_{1.2\text{mm}} \lesssim 0.05$ mJy the SMG differential number counts cannot keep rising with the faint-end slope observed for $S_{1.2\text{mm}} > 0.05$ mJy, and that the bright SMG population contributes at most a small fraction to the 1.2 mm CIB.

The high resolution afforded by the IRAM 30 m telescope, the large extent of our map, and the use of analysis methods that thoroughly take into account the negative residuals of the chopped triple-beam PSF have allowed us to demonstrate possible clustering in the 1.2 mm population. The SMG correlation function, a nearest neighbors analysis, and, to a lesser extent, the spatial correlation of our significant detections with large radio sources over the same redshift range all suggest that our sample traces some degree of large scale structure at high redshift. Our work prepares the 1.2 mm waveband for the ALMA era by creating a better understanding of this population's statistical properties and setting new 1.2 mm constraints for galaxy evolution models.

We thank the scientific and technical staff at IRAM, particularly Robert Zylka, as well as several seasons' pool observers, for their help in making this project a success. We thank Jacqueline Bergeron, David Hughes, Chuck Keeton, Maurilio Pannella, and Jean Walker for useful discussions.

We also thank the referee for very useful comments that have improved the analysis and results of this paper. This project has been supported by NSF grant AST-0708653.

Facilities: IRAM, VLA, SST, GMRT.

A. Notes on individual detections

A.1. MM J104700.1+590109 = ID # 1

Polletta et al. (2006) report an optical $z_{\text{spec}} = 2.562$ for this source. It also has a $70\ \mu\text{m}$ counterpart with $S_{70\ \mu\text{m}} = 10.4 \pm 1.7\ \text{mJy}$ at a distance of $3.2''$, and a $160\ \mu\text{m}$ counterpart with $S_{160\ \mu\text{m}} = 24.1 \pm 1.9\ \text{mJy}$ at a distance of $1.7''$ (Owen et al. 2011b).

A.2. MM J104631.4+585056 = ID # 3

In addition to the robust 20 cm counterpart listed in Table 2, this source has an additional likely counterpart with $S_{20\ \text{cm}} = 30\ \mu\text{Jy}$, separation $2.6''$, and $P = 0.034$, with which it is nearly blended. Neither radio counterpart has an estimated photometric redshift. Figure 22 shows 1.2 mm contours overlaid on a 20 cm cutout image that includes both counterparts.

A.3. MM J104638.4+585613 = ID # 6

We identify this source with LHN8 in the *Herschel* catalog of Magdis et al. (2010), from which it is separated by $2.0''$ ($P = 0.0084$), and with SWIRE4_LJ104638.68+585612.5 = ID # L14 in the *Spitzer* sample of Fiolet et al. (2010), who report a mid-IR $z_{\text{spec}} = 2.03$. Fiolet et al. (2009) report an on-off flux density measurement of $S_{1.2\ \text{mm}} = 2.13 \pm 0.71\ \text{mJy}$, which is consistent with our (non-deboosted) $S_{1.2\ \text{mm}} = 2.7 \pm 0.5\ \text{mJy}$ within the uncertainties.

A.4. MM J104704.9+585008 = ID # 9

The radio counterpart to this source ($P = 0.0043$) is not in the catalog of Owen & Morrison (2008) because it has a S/N ratio of 4.8.

A.5. MM J104556.5+585317 = ID # 11

We identify this source with LHN1 in the *Herschel* catalog of Magdis et al. (2010), from which it is separated by $3.4''$ ($P = 0.0057$), and with SWIRE4_LJ104556.90+585318.8 = ID # L11 in the *Spitzer* sample of Fiolet et al. (2010), who report a mid-IR $z_{\text{spec}} = 1.95$ in good agreement with the optical $z_{\text{phot}} = 1.80$ reported by Strazzullo et al. (2010). Fiolet et al. (2009) report an on-off flux density measurement of $S_{1.2\ \text{mm}} = 3.08 \pm 0.58\ \text{mJy}$, which is consistent with our (non-deboosted) $S_{1.2\ \text{mm}} = 3.4 \pm 0.6\ \text{mJy}$ within the uncertainties. This source also has a $160\ \mu\text{m}$ counterpart (Owen et al. 2011b) with $S_{160\ \mu\text{m}} = 11.8 \pm 1.5\ \text{mJy}$ at a distance of $4.3''$.

A.6. MM J104728.3+585213 = ID # 15

This source has two radio counterparts; the primary counterpart listed in Table 2 has $z_{\text{phot}} = 2.76$, while the second (with $P = 0.032$) has $z_{\text{phot}} = 1.06$. In the 20 cm map, we see a quadruple radio source (see Figure 23). At a low level of significance, the 1.2 mm emission appears to be elongated in the same direction as the radio source(s). This system also has a $160\ \mu\text{m}$ counterpart (Owen et al. 2011b) with $S_{160\ \mu\text{m}} = 12.7 \pm 1.5\ \text{mJy}$ at a distance of $6.8''$.

A.7. MM J104610.4+590242 = ID # 17

This source is separated by only $\sim 15''$ from MM J104611.9+590231 = ID # 39. The catalog of Owen & Morrison (2008) includes a single radio source whose nominal position is midway between two very faint sources (one resolved, one unresolved) that are visible in the original 20 cm map (see Figure 24). These two sources, with peak flux densities of $15.6\ \mu\text{Jy}$ and $13.5\ \mu\text{Jy}$, are only identifiable because they lie very close to the center of the VLA map, where the local RMS noise is only $2.9\ \mu\text{Jy beam}^{-1}$. After attributing the flux of the catalogued source to its two constituents, we find that one is a robust radio counterpart

for the MAMBO source (1.0'' separation with $P = 0.0099$), while the other is probably a chance association (3.3'' separation with $P = 0.077$).

A.8. MM J104617.0+585444 = ID # 20

This source has an unlikely 20 cm radio counterpart ($P = 0.12$) with $S/N = 4.2$ ($S_{20\text{ cm}} = 15.0 \pm 3.6 \mu\text{Jy}$), and is therefore not in the catalog of Owen & Morrison (2008), which includes only sources with $S/N > 5.0$.

A.9. MM J104522.8+585558 = ID # 26

This source has no radio counterpart within 8'' and no likely 24 μm counterpart, although it does have an X-ray counterpart (see §6.5).

A.10. MM J104620.9+585434 = ID # 28

This source has a likely 20 cm radio counterpart ($P = 0.029$) with $S/N = 4.3$ ($S_{20\text{ cm}} = 24.8 \pm 5.8 \mu\text{Jy}$), and is therefore not in the catalog of Owen & Morrison (2008), which includes only sources with $S/N > 5.0$.

A.11. MM J104556.1+590914 = ID # 29

We identify this source with SDSS J104555.49+590915.9, an optically bright galaxy for which Owen & Morrison (2009a) report an optical $z_{\text{spec}} = 0.044$. Figure 25 shows a red optical image overlaid with 1.2 mm contours, which at a low level of significance are elongated in the same direction as the galaxy's stars. This $\simeq 20''$ source is heavily resolved at 20 cm and 50 cm. It is also detected at 160 μm (Owen et al. 2011b) with $S_{160\text{ }\mu\text{m}} = 15.8 \pm 1.4 \text{ mJy}$ (at a separation of 6.6''), and at 250 μm (*Herschel*/SPIRE; Smith et al. 2011) with $S_{250\text{ }\mu\text{m}} = 133 \pm 8 \text{ mJy}$ (at a separation of 3.6'').

A.12. MM J104539.6+585419 = ID # 32

We identify this source with LHN3 in the *Herschel* catalog of Magdis et al. (2010), from which it is separated by 5.2'' ($P = 0.016$). Magdis et al. (2010) estimate $z'_{\text{phot}} = 2.40$ on the basis of their PACS and SPIRE photometry, which we list in Table 2 rather than the Strazzullo et al. (2010) optical $z_{\text{phot}} = 1.32$, due to the close connection between far-IR and millimeter emission.

A.13. MM J104608.1+590744 = ID # 36

This source has a 20 cm radio counterpart ($P = 0.041$) with $S/N = 4.9$ ($S_{20\text{ cm}} = 16.1 \pm 3.3 \mu\text{Jy}$), and is therefore not in the catalog of Owen & Morrison (2008), which includes only sources with $S/N > 5.0$.

A.14. MM J104610.8+585242 = ID # 37

We identify this source with LHN4 in the *Herschel* catalog of Magdis et al. (2010), from which it is separated by 2.4'' ($P = 0.013$). Magdis et al. (2010) estimate $z'_{\text{phot}} = 1.72$ on the basis of their PACS and SPIRE photometry, which we list in Table 2; this is in good agreement with the optical $z_{\text{phot}} = 1.66$ reported by Strazzullo et al. (2010).

A.15. MM J104611.9+590231 = ID # 39

This source is separated by only $\sim 15''$ from MM J104610.4+590242 = ID # 17. It also has a pair of likely radio counterparts within an 8'' search radius. Figure 24 shows 1.2 mm contours overlaid on a 20 cm cutout image. This source is not identified in the catalog of Owen & Morrison (2008).

REFERENCES

- Adler, R. J., 1981, *The Geometry of Random Fields* (Chichester: Wiley)
- Alexander, D. M., et al. 2003, *AJ*, 125, 383
- Alexander, D. M., Bauer, F. E., Chapman, S. C., Smail, I., Blain, A. W., Brandt, W. N., Ivison, R. J. 2005, *ApJ*, 632, 736
- Austermann, J. E., et al. 2009, *MNRAS*, 393, 1573
- Austermann, J. E., et al. 2010, *MNRAS*, 401, 160
- Barger, A. J., Cowie, L. L., Sanders, D. B., Fulton, E., Taniguchi, Y., Sato, Y., Kawara, K., Okuda, H. 1998, *Nature*, 394, 248
- Baugh, C. M., Lacey, C. G., Frenk, C. S., Granato, G. L., Silva, L., Bressan, A., Benson, A. J., Cole, S. 2005, *MNRAS*, 356, 1191
- Béthermin, M., Dole, H., Beelen, A., Aussel, H. 2010, *A&A*, 512, id.A78
- Béthermin, M., Dole, H., Lagache, G., Le Borgne, D., Pénin, A. 2011, *A&A*, 529, 4
- Bertoldi, F., et al. 2007, *ApJS*, 172, 132
- Best, P. N., 2004, *MNRAS*, 351, 70
- Best, P. N., Kauffmann, G., Heckman, T. M., Brinchmann, J., Charlot, S., Ivezić, Ž., White, S. D. M. 2005, *MNRAS*, 362, 25
- Biggs A. D., et al. 2011, *MNRAS*, 413, 2314
- Blain, A. W., Smail, I., Ivison, R. J., Kneib, J. P., Frayer, D. T. 2002, *Phys. Rev.*, 369, 111
- Borys, C., Chapman, S., Halpern, M., Scott, D. 2003, *MNRAS*, 344, 385
- Borys, C., Scott, D., Chapman, S., Halpern, M., Nandra, K., Pope, A. 2004, *MNRAS*, 355, 485
- Carilli, C. L. & Yun, M. S. 1999, *ApJ*, 513, L13
- Carilli, C. L. & Yun, M. S. 2000, *ApJ*, 530, 618
- Chapin, E. L., et al. 2009, *MNRAS*, 398, 1793
- Chapman, S. C., Blain, A. W., Ivison, R. J., Smail, I. 2003, *Nature*, 422, 695
- Chapman, S. C., Blain, A. W., Smail, I., Ivison, R. J. 2005, *ApJ*, 622, 772
- Chapman, S. C., Smail, I., Blain, A. W., Ivison, R. J. 2004, *ApJ*, 614, 671
- Chapman, S. C., et al. 2010, *MNRAS*, 409, L13
- Conselice, C. J., Chapman, S. C., Windhorst, R. A. 2003, *ApJ*, 596, L5
- Condon, J. J. 1974, *ApJ*, 188, 279
- Condon, J. J., Cotton, W. D., Greisen, E. W., Yin, Q. F., Perley, R. A., Taylor, G. B., & Broderick, J. J. 1998, *AJ*, 115, 1693
- Condon, J. J., 1992, *ARA&A*, 30, 575
- Coppin, K., et al. 2006, *MNRAS*, 372, 1621
- Coppin, K., Halpern, M., Scott, D., Borys, C., Chapman, S. 2005, *MNRAS*, 357, 1022
- Davé, R., Finlator, K., Oppenheimer, B. D., Fardal, M., Katz, N., Kereš, D., Weinberg, D. H. 2010, *MNRAS*, 404, 1355
- Dole, H., et al. 2006, *A&A*, 451, 417
- Downes, A. J. B., Peacock, J. A., Savage, A., & Carrie, D. R. 1986, *MNRAS*, 218, 31
- Fiolet, N., et al. 2009, *A&A*, 508, 117
- Fiolet, N., et al. 2010, *A&A*, 524, id.A33
- Fixsen, D. J., Dwek, E., Mather, J. C., Bennett, C. L., Shafer, R. A. 1998, *ApJ*, 508, 123
- Frayer, D. T., Ivison, R. J., Scoville, N. Z., Yun, M., Evans, A. S., Smail, I., Blain, A. W., Kneib, J. -P. 1998, *ApJ*, 506, L7
- Frayer, D. T., et al. 1999, *ApJ*, 514, L13
- Gawiser, E., et al. 2006, *ApJS*, 162, 1
- Gehrels, N. 1986, *ApJ*, 303, 336
- Glenn, J., et al. 2010, *MNRAS*, 409, 109
- Greve, T. R., Ivison, R. J., Bertoldi, F., Stevens, J. A., Dunlop, J. S., Lutz, D., & Carilli, C. L. 2004, *MNRAS*, 354, 779
- Greve, T. R., et al. 2005, *MNRAS*, 359, 1165

- Greve, T. R., Pope, A., Scott, D., Ivison, R. J., Borys, C., Conselice, C. J., & Bertoldi, F. 2008, *MNRAS*, 389, 1489
- Hatsukade, B., et al. 2011, *MNRAS*, 411, 102
- Hayward, C. C., Kereš, D., Jonsson, P., Narayanan, D., Cox, T. J., Hernquist, L. 2011, *ApJ*, submitted (arXiv:1101.0002)
- Hill, G. J., & Lilly, S. J. 1991, *ApJ*, 367, 1
- Hogg, D. W. & Turner, E. L. 1998, *PASP*, 110, 727
- Holland, W. S., et al., 1999, *MNRAS*, 303, 659
- Hughes, D. H., et al. 1998, *Nature*, 394, 241
- Ibar, E., Ivison, R. J., Biggs, A. D., Lal, D. V., Best, P. N., Green, D. A. 2009, *MNRAS*, 397, 281
- Ibar, E., Ivison, R. J., Best, P. N., Coppin, K., Pope, A., Smail, I., Dunlop, J. S. 2010, *MNRAS*, 401, L53
- Ivison, R. J., Smail, I., Le Borgne, J. -F., Blain, A. W., Kneib, J. -P., Bezecourt, J., Kerr, T. H., Davies, J. K. 1998, *MNRAS*, 298, 583
- Ivison, R. J., et al. 2002, *MNRAS*, 337, 1
- Ivison, R. J., Smail, I., Barger, A. J., Kneib, J. -P., Blain, A. W., Owen, F. N., Kerr, T. H., Cowie, L. L. 2000, *MNRAS*, 315, 209
- Ivison, R. J., et al. 2005, *MNRAS*, 364, 1025
- Ivison, R. J., et al. 2007, *MNRAS*, 380, 199
- Klein, U., Wielebinski, R., Morsi, H. W. 1988, *A&A*, 190, 41
- Knudsen, K. K., van der Werf, P. P., & Kneib, J.-P. 2008, *MNRAS*, 384, 1611
- Kreysa, E., et al. 1998, *Proc. SPIE*, 3357, 319
- Landy, S. D. & Szalay, A. S. 1993, *ApJ*, 412, 64
- Laurent, G. T., et al. 2005, *ApJ*, 623, 742
- Lonsdale, C. J., et al. 2003, *PASP*, 115, 897
- Maloney, P. R., et al. 2005, *ApJ*, 635, 1044
- Magdis, G. E., et al. 2010, *MNRAS*, 409, 22
- Magnelli, B., et al. 2010, *A&A*, 518, L28
- Markwardt, C. B. 2008, *ASP Conference Series*, 411, 251
- Marsden, G., et al. 2011, *MNRAS*, submitted (arXiv:1010.1176)
- Menéndez-Delmestre, K., et al. 2007, *ApJ*, 655, L65
- Menéndez-Delmestre, K., et al. 2009, *ApJ*, 699, 667
- Narayanan, D., Cox, T., Hayward, C., Younger, J., Hernquist, L. 2009, *MNRAS*, 400, 1919
- Narayanan, D., Hayward, C., Cox, T., Hernquist, L., Jonsson, P., Younger, J., Groves, B. 2010, *MNRAS*, 401, 1613
- Neri, R., et al. 2003, *ApJ*, 597, L113
- Oliver, S. J., et al. 2010, *A&A*, 518, L21
- Owen, F. N., et al. 2011a, in preparation
- Owen, F. N., et al. 2011b, in preparation
- Owen, F. N. & Morrison, G. E. 2008, *AJ*, 136, 1889
- Owen, F. N. & Morrison, G. E. 2009, *ApJS*, 182, 625
- Owen, F. N., Morrison, G. E., Klimek, M. D., & Greisen, E. W. 2009, *AJ*, 137, 4846
- Patanchon, G., et al. 2009, *ApJ*, 707, 1750
- Penner, K., et al. 2011, *MNRAS*, 410, 2749
- Perera, T. A., et al. 2008, *MNRAS*, 391, 1227
- Polletta, M., et al. 2006, *ApJ*, 642, 673
- Pope, A. et al. 2006, *MNRAS*, 370, 1185
- Pope, A., et al. 2008, *ApJ*, 675, 1171
- Puget, J. L. Abergel, A., Bernard, J. -P., Boulanger, F., Burton, W. B., Desert, F. -X., Hartmann, D. 1996, *A&A*, 308, L5
- Rowan-Robinson, M. 2009, *MNRAS*, 394, 117
- Schechter, P. 1976, *ApJ*, 203, 297
- Schinnerer, E., et al. 2007, *ApJS*, 172, 46

- Scott, D., & Tout, C. A., 1989, MNRAS, 241, 109
- Scott, S. E., Dunlop, J. S., Serjeant, S. 2006, MNRAS, 370, 1057
- Scott, K. S., et al. 2008, MNRAS, 385, 2225
- Scott, K. S., et al. 2010, MNRAS, 405, 2260
- Scoville, N. Z., Sargent, A. I., Sanders, D. B., Soifer, B. T. 1991, ApJ
- Serjeant, S., et al. 2003, MNRAS, 344, 887
- Smail, I., Ivison, R. J., Blain, A. W. 1997, ApJ, 490, L5
- Smith, A., et al. 2011, in preparation
- Strazzullo, V., Pannella, M., Owen, F. N., Bender, R., Morrison, G. E., Wang, W.-H., & Shupe, D. L. 2010, ApJ, 714, 1305
- Tacconi, L. J., et al. 2006, ApJ, 640, 228
- Valiante, E., Lutz, D., Sturm, E., Genzel, R., Tacconi, L. J., Lehnert, M. D., Baker, A. J. 2007, ApJ, 660, 1060
- Valiante, E., et al. 2010, ApJS, 191, 222
- Valiante, E., Lutz, D., Sturm, E., Genzel, R., Chapin, E. L. 2009, ApJ, 701, 1814
- Voss, H., Bertoldi, F., Carilli, C., Owen, F. N., Lutz, D., Holdaway, M., Ledlow, M., Menten, K. M. 2006, A&A, 448, 823
- Wake, D. A., Croom, S. M., Sadler, E. M., Johnston, H. M. 2008, MNRAS, 391, 1674
- Wardlow, J. L., et al. 2011, MNRAS, submitted (arXiv:1006.2137)
- Wei, A., et al. 2009, ApJ, 707, 1201
- Wilkes, B., et al. 2009, ApJS, 185, 433
- Williams, C. C., et al. 2011, ApJ, 733, 92
- Yun, M. S. & Carilli, C. L. 2002, ApJ, 568, 88

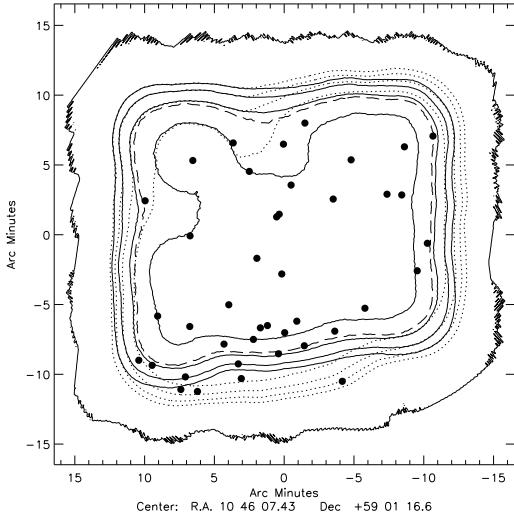


Fig. 1.— Weight map. Contours denote post-filtering RMS noise levels of 0.8, 1.0, 1.2, and 1.4 mJy beam^{-1} in the “best” data (solid contours) and the “full” data (dotted contours). Thick dashed contour shows the map region used for the $P(D)$ analysis of the “best” data. Circles show the locations of detected sources with $S/N \geq 4.0$. The thick outer edge shows the extent of the full map. The effective areas comprising the “best” and “full” maps (RMS noise $< 1.5 \text{ mJy beam}^{-1}$ after filtering) are 514 and 566 arcmin^2 , respectively.

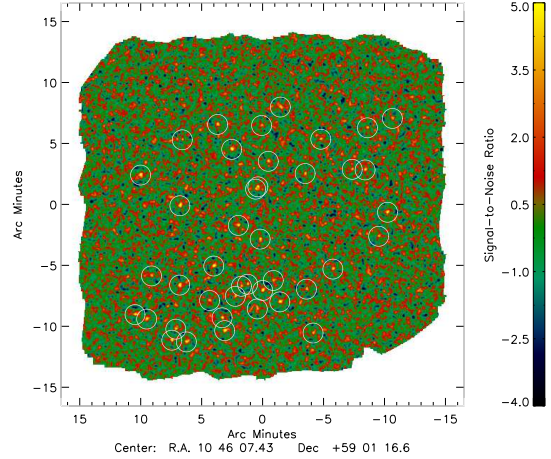


Fig. 2.— The complete, optimally filtered S/N map of the “full” dataset, with white circles showing the locations of our 41 detections with $S/N > 4.0$.

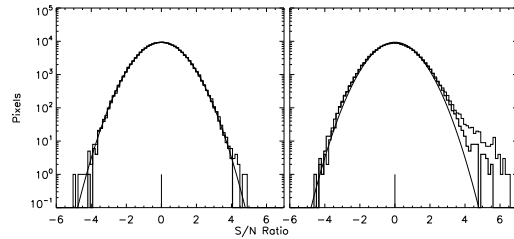


Fig. 3.— Pixel flux distributions of the S/N maps. Left: Histograms are shown for both shuffled (thin) and jackknifed (thick) noise maps. Right: S/N map histogram for the “best” map (thick) and the “full” map (thin). Over-plotted in both panels is a Gaussian function with unit standard deviation and zero mean, normalized to the area under the histograms. All maps have a mean value consistent with zero (shown as the vertical line segment), enforced by the chopped observing mode of the IRAM 30 m telescope and SAA reconstruction. The “full” map has more pixels with high S/N because it reaches a higher sensitivity. The histograms were created with maps trimmed to a noise level of $1.5 \text{ mJy beam}^{-1}$.

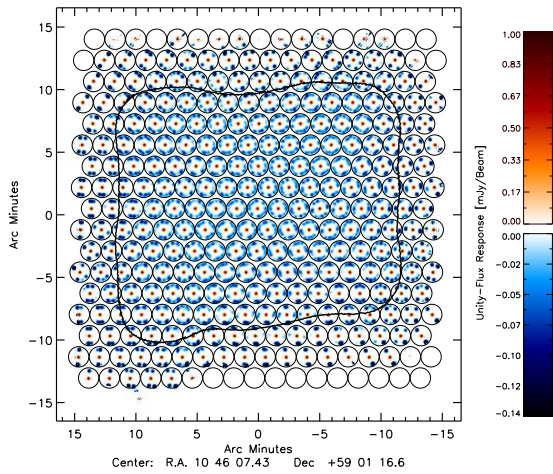


Fig. 4.— The effective PSF (including negative residuals) as a function of position across our “best” map. Red/blue represents a positive/negative signal response. The thick solid contour encloses the area where the “best” map has RMS noise $< 1.5 \text{ mJy beam}^{-1}$.

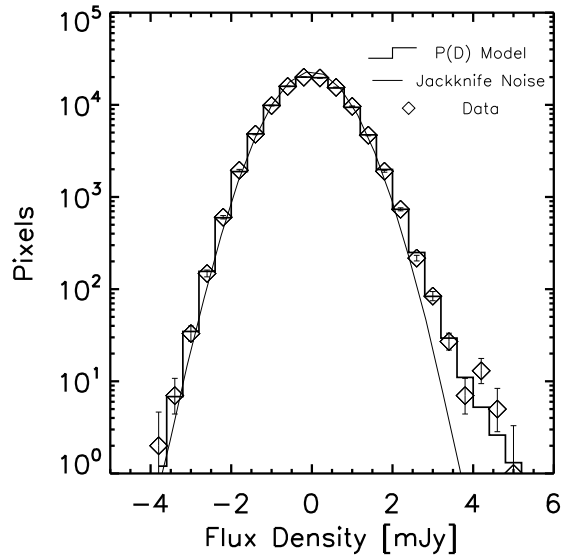


Fig. 5.— Pixel flux distribution showing the agreement between the data and the average best-fit (Schechter function) model from the $P(D)$ analysis. Points represent the PFD of the optimally filtered “best” data. The solid histogram shows the mean PFD of 100 random sky realizations of the best fitting number counts embedded in random jackknifed noise maps. The thin curve represents the mean histogram of only the jackknifed noise maps. The single larger flux density bin that spanned 4–5 mJy for the $P(D)$ analysis (see §4) is shown here broken down into small bins matching the rest of the distribution.

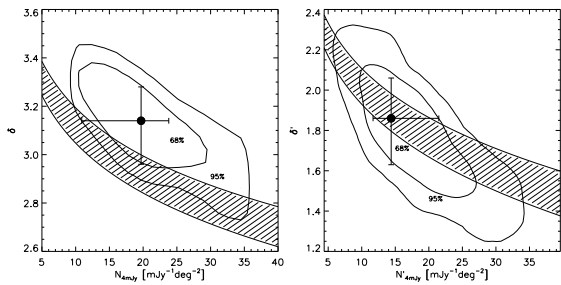


Fig. 6.— Likelihood parameter spaces for different parametrizations of the 1.2 mm differential number counts. The points mark the best fitting parameters and the marginalized 68% double-sided error bars. The contours bound the 68% and 95% confidence regions found through Monte Carlo simulations. The shaded bands show the regions in parameter space that reproduce the observed intensity of the 1.2 mm CIB, assuming a lower-limit flux density cutoff of 0.05 mJy. *Left*: Power law model, with best fitting parameters $N_{4 \text{ mJy}} = 19.7^{+4.1}_{-8.8} \text{ deg}^{-2} \text{ mJy}^{-1}$ and $\delta = 3.14^{+0.14}_{-0.18}$. *Right*: Schechter function model, with best fitting parameters $N'_{4 \text{ mJy}} = 14.5^{+7.1}_{-2.7} \text{ deg}^{-2} \text{ mJy}^{-1}$ and $\delta' = 1.86^{+0.20}_{-0.23}$.

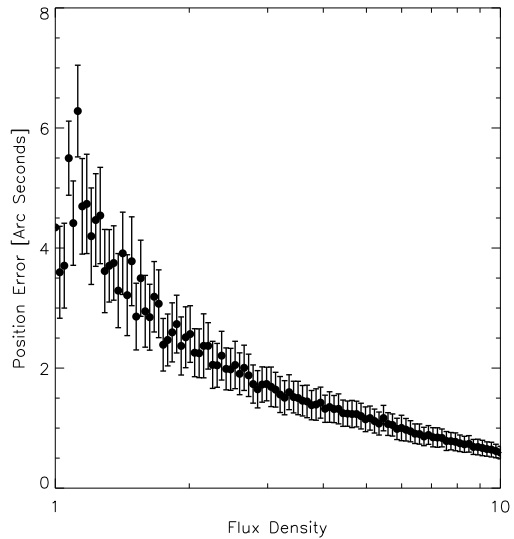


Fig. 7.— Average angular separation between injected and recovered source locations as a function of flux density. The injection process was performed 1000 times for each flux density value. The scatter increases at low flux densities because of incompleteness.

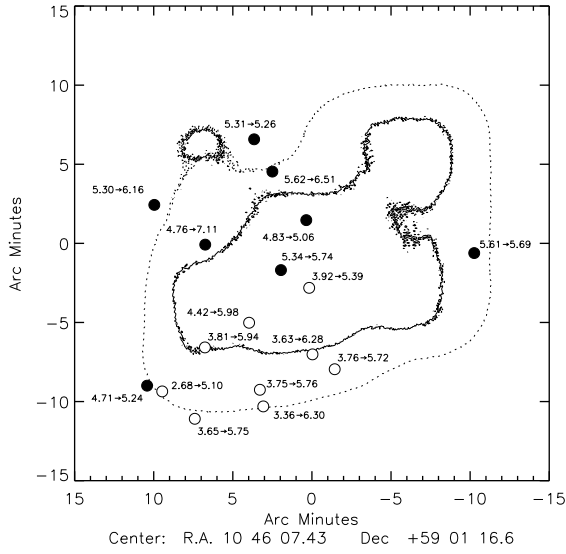


Fig. 8.— The change in S/N of our 17 comparison sources in the “best” and “full” datasets. Filled circles show eight sources in the “best” map with $S/N \geq 4.5$. In the “full” map, we recover all of these detections, plus others shown as empty circles, above a threshold $S/N \geq 5.0$. The solid/dashed contour denotes the 1 mJy beam^{-1} RMS noise threshold in the maps of the “best”/“full” data. The numbers near each detection show the S/N ratio of that source in the “best” data \rightarrow “full” data.

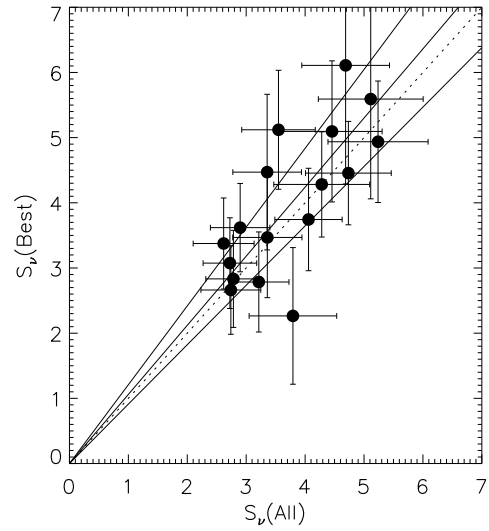


Fig. 9.— Flux density comparison between the 17 highest S/N detections in the “full” data and their counterparts in the “best” data (these sources are plotted in Figure 8). The solid lines show the best fit slope with 2σ uncertainties of a line constrained to cross the origin. For illustration, the dotted line has unit slope. The chi-square minimization with x and y errors was performed using the IDL script `mpfit.pro` (Markwardt 2008). The best fitting slope is $m = 1.06 \pm 0.07$ ($\pm 1\sigma$ uncertainties).

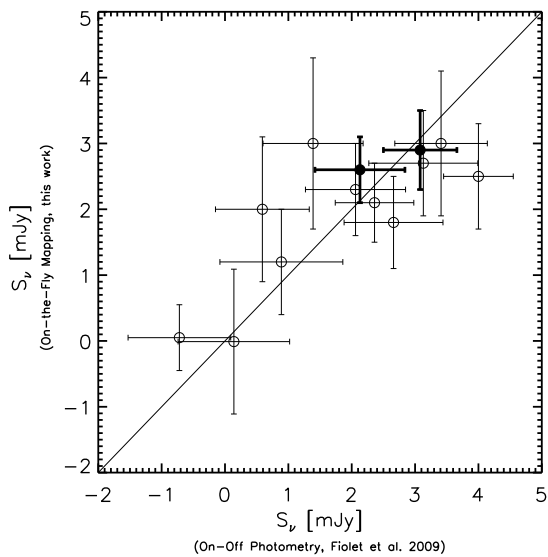


Fig. 10.— Flux density comparison between on-off photometry-mode (Fiolet et al. 2009) and on-the-fly mapping (this work) of 13 *Spitzer*-selected starburst galaxies in the LHN that lie within our “full” map coverage. Symbols with thick (thin) lines represent 2 (11) of the sources from Fiolet et al. (2009) with significant detections (non-detections) in our full map.

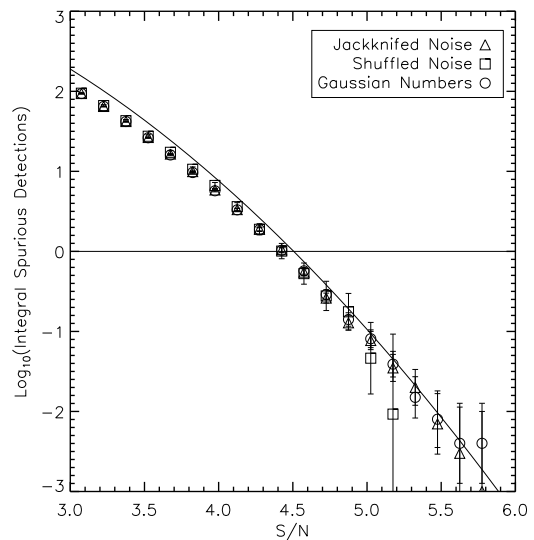


Fig. 11.— Integral numbers of spurious detections as a function of S/N within jackknifed noise maps, shuffled noise maps, and maps of random Gaussian numbers. We expect to detect 0.8 spurious sources with $S/N \geq 4.5$ and $\simeq 5.4$ spurious sources with $S/N \geq 4.0$. The curve shows the expected number of excursions above a given S/N level within a Gaussian random field in the limit of high S/N (Adler 1981).

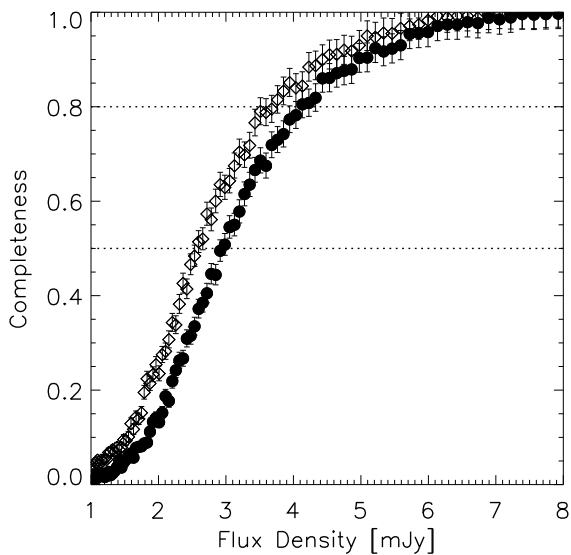


Fig. 12.— Completeness as a function of flux density. The circles/diamonds represent $4.5\sigma/4.0\sigma$ source extraction thresholds for detection. The number count calculation uses a threshold of 4.5σ , while our source catalog includes sources down to 4.0σ . Horizontal lines represent 80% and 50% completeness limits.

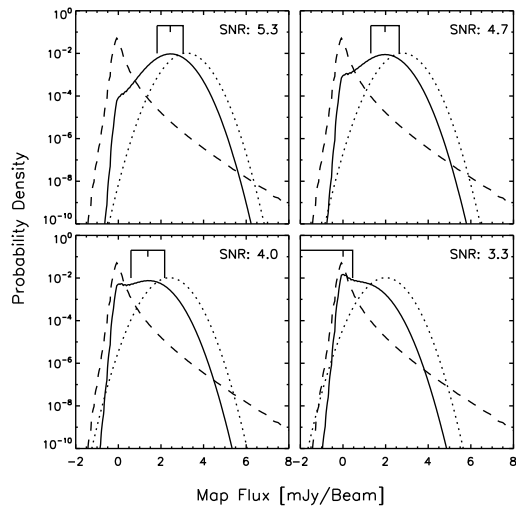


Fig. 13.— Posterior probability distributions of four characteristic S/N regimes. The dotted lines represent the Gaussian probability distributions for each of the four measurements (the likelihoods), all assuming $\sigma = 0.6$ mJy and varying mean. The dashed lines represent the prior flux distribution constructed from Monte Carlo simulations, and the solid lines represent the the normalized posterior probability distributions. The brackets above the curves denote the peak likelihood values (the deboosted flux densities) along with the left and right 38% confidence intervals. When the S/N is too low for either the left or the right confidence interval to converge, as is the case in the final panel, we use instead the analytic formula from Equation 12.

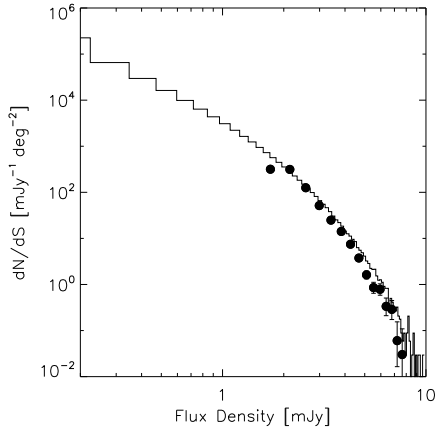


Fig. 14.— Monte Carlo simulation to test our Bayesian flux boosting correction. The histogram shows the average number counts model used to inject sources into realistic noise maps. The circles show the average number counts calculated from the raw counts by using the Bayesian method to deboost the flux density of each recovered source. Error bars represent only the Poisson uncertainty in the average (Gehrels 1986).

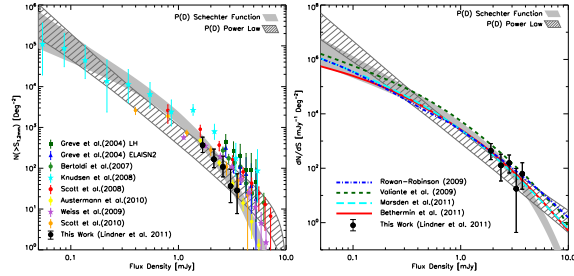


Fig. 15.— *Left*: 1.2 mm integral number counts, compared to the $P(D)$ analysis best fit models and other observed number counts from the literature. Filled black circles show our Bayesian deboosted number counts with 95% confidence error bars including the Poisson uncertainty and the uncertainty in the completeness correction. The solid filled region shows the 95% confidence region for the best fitting Schechter function from the $P(D)$ analysis. The cross-hatched region shows the same for the best fitting power law. MAMBO counts: LH and ELAIS-N2 (green squares and blue triangles; Greve et al. 2004), COSMOS (green circles; Bertoldi et al. 2007). LABOCA counts: ECDF-S (purple stars; Weiß et al. 2009). AzTEC counts: GOODS-S (orange circles; Scott et al. 2010), SHADES (yellow circles; Austermann et al. 2010), COSMOS (red circles; Scott et al. 2008). SCUBA lensing cluster counts from Knudsen et al. (2008) are shown as red stars. The counts at 850 μm (SCUBA), 870 μm (LABOCA), and 1.1 mm (AzTEC) have been scaled to 1.2 mm (see §7.1). *Right*: 1.2 mm differential number counts and $P(D)$ models compared to the predictions of galaxy evolution models. Lines represent different differential counts predictions by Rowan-Robinson (2009), blue dot-dashed; Valiante et al. (2009), green short-dashed; Béthermin et al. (2011), red solid; Marsden et al. (2011), cyan long-dashed. Models with predictions only for the 1.1 mm waveband were scaled in order to compare to our observations (see §7.1).

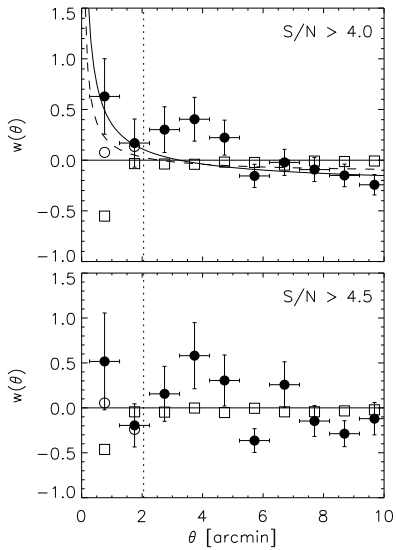


Fig. 16.— Landy-Szalay correlation function estimator $w(\theta)$ as a function of angular separation. Top panel uses our 41 detections with $S/N > 4.0$. Bottom panel uses 27 sources with $S/N > 4.5$. The vertical dashed line shows upper limit in θ on the clustering suppression effect introduced by chopping (see §5.8). Open squares show the results from using random positions to check the zero-clustering baseline; open circles show the raw clustering signal, which are corrected for the zero-clustering baseline to deliver the filled circles.

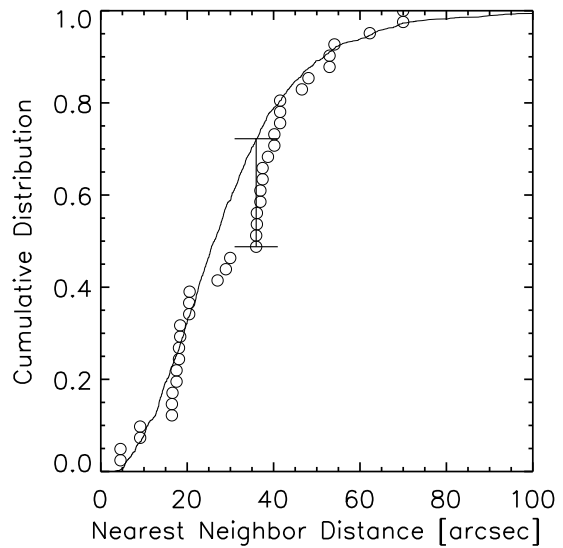


Fig. 17.— Integral distribution of nearest neighbors. Solid line shows the distribution from Monte-Carlo generated random positions. Circles show the distribution of our 41 significant detections. The vertical line segment denotes the maximum difference between the two distributions. A Kolmogorov-Smirnov test rules out the hypothesis that our sources are drawn from a random distribution at 95% confidence.

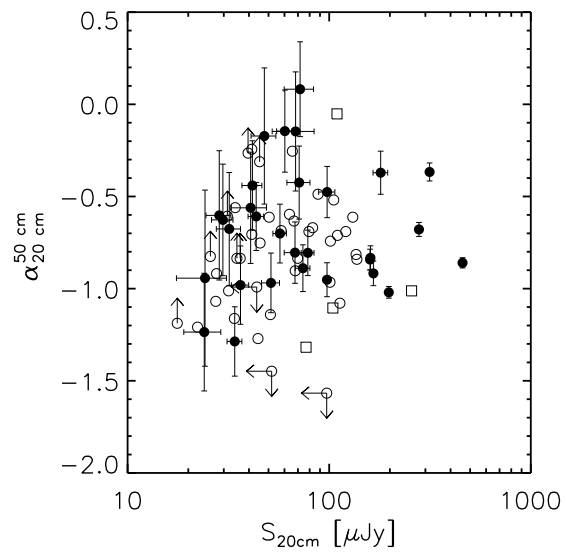


Fig. 18.— 50/20 cm spectral index vs. 20 cm flux density for SMG radio counterparts. Solid circles represent the 20 unblended 50 cm radio counterparts to our MAMBO detections. Open circles (squares) represent non AGN-dominated (AGN-dominated) SMGs in the LHE field (Ibar et al. 2010).

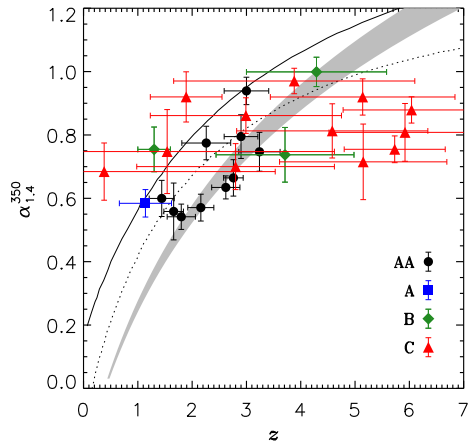


Fig. 19.— 350/1.4 GHz spectral index ($\alpha_{1.4}^{350}$) vs. z . Black circles, blue squares, green diamonds, and red triangles have z_{phot} with fit qualities of AA, A, B, and C, respectively. The shaded area shows the expected behavior of $\alpha_{1.4}^{350}$ for the Carilli & Yun (1999) spectral index redshift indicator, with $-\alpha_{\text{radio}}$ ranging from 0.52–0.80. The solid and dashed lines show the empirical relations obtained by redshifting the SEDs of nearby starburst galaxies Arp 220 and M82, respectively.

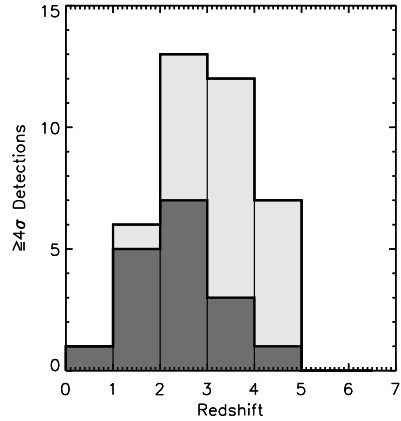


Fig. 20.— Redshift distribution of significant detections. The light grey histogram includes all sources. The dark grey histogram includes only sources with spectroscopic or high-quality (*Herschel* or AA/A/B-grade optical) photometric redshifts.

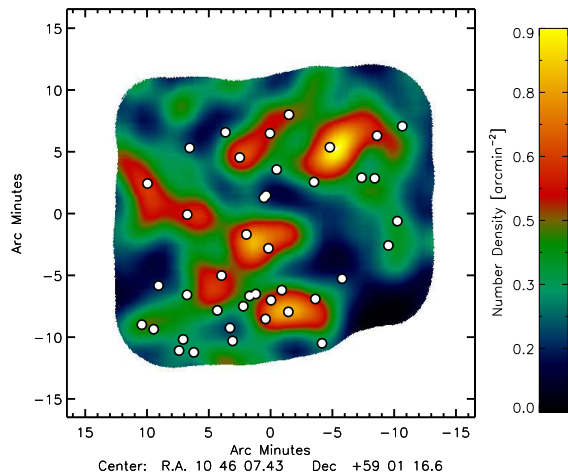


Fig. 21.— Distributions of individually detected MAMBO sources and the smoothed surface density of 20 cm radio sources with $1.5 < z_{\text{phot}} < 4.5$ (excluding radio sources with C-quality photometric redshifts) and sizes $\geq 1''$. The area shown is the region in the “full” map used for source extraction.

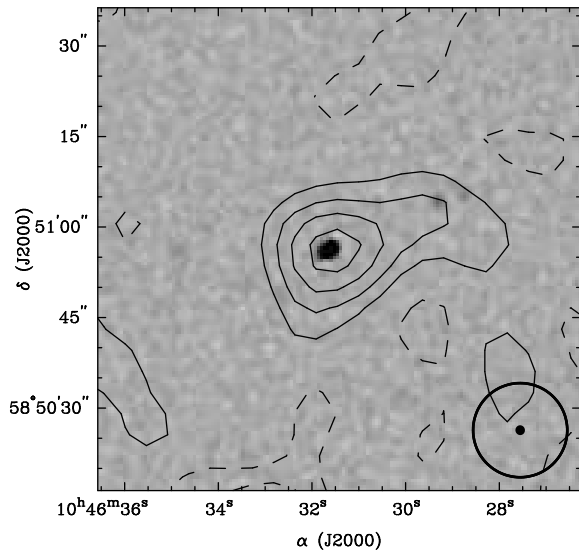


Fig. 22.— 1.2 mm contours (multiples of $1.0 \text{ mJy beam}^{-1}$) for MAMBO source MM J104631.4+585056 = ID # 03, overlaid on 20 cm map showing double counterpart. The black circle and small filled ellipse at lower right represent the $15.6''$ MAMBO beam (after filtering) and the $1.63'' \times 1.57''$ VLA beam, respectively.

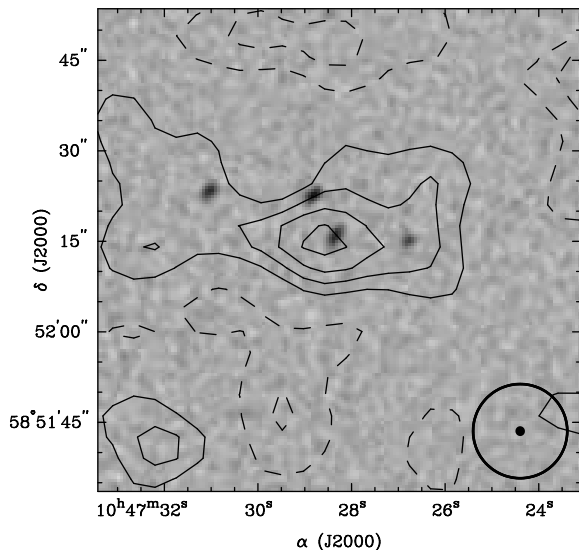


Fig. 23.— 1.2 mm contours (multiples of $1.0 \text{ mJy beam}^{-1}$) for MAMBO source MM J104728.3+585213 = ID # 15, overlaid on 20 cm map showing multiple counterparts. Other notation is as in Figure 22.

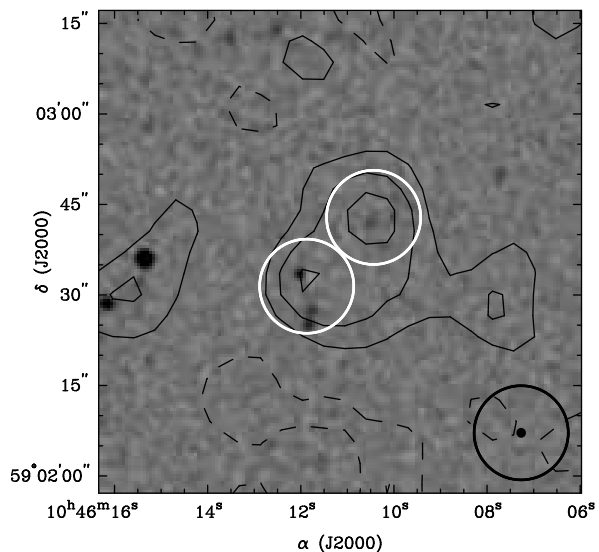


Fig. 24.— Nearly blended MAMBO sources MM J104610.4+590242 (ID # 17), which has one likely 20 cm counterpart, and MM J104611.9+590231 (ID # 39), which has two likely 20 cm counterparts. 1.2 mm contours (multiples of $0.7 \text{ mJy beam}^{-1}$) are overlaid on 20 cm greyscale. White circles are centered on the positions of the extracted MAMBO sources; other notation is as in Figure 22.

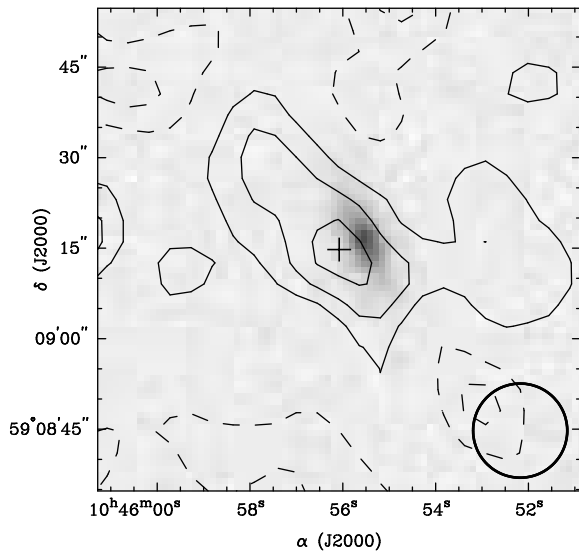


Fig. 25.— 1.2 mm contours (multiples of $0.8 \text{ mJy beam}^{-1}$) for MAMBO source MM J104556.1+590914 = ID # 29, overlaid on a DSS red image of SDSS J104555.49+590915.9 at $z_{\text{spec}} = 0.044$ (Owen & Morrison 2009a). Other notation is as in Figure 22.

TABLE 1
MAMBO OBSERVATIONS

Season	Maps	Hours	Tracking jitter?	Bad refraction correction?	Chop throws (arcsec)
2006 winter	76	78.9	X	X	36/48
2008 summer	12	12.3	X		42/36
2008 winter	39	40.3			42/36
2009 summer	8	8.0			42/36
2009 winter	52	53.0			42/36
Total “best”	99	101.3			
Total “full”	183	192.5			

NOTE.—“Best” data use maps from winter 2008, summer 2009, and winter 2010. “Full” data use maps from all seasons in the table.

TABLE 2
MAMBO DETECTIONS

ID	Source name	$S_{\nu}^{\text{Best}^a}$ (mJy)	$S_{\nu}^{\text{Full}^b}$ (mJy)	$S_{\nu}^{\text{Deboosted}^c}$ (mJy)	$P(< 0)^d$	z	$D_{20\text{ cm}}^e$ (arcsec)	$P_{20\text{ cm}}^f$	$S_{20\text{ cm}}^g$ (μJy)	$S_{50\text{ cm}}^h$ (μJy)	$S_{90\text{ cm}}^i$ (μJy)	$P_{24\text{ }\mu\text{m}}^j$	$S_{24\text{ }\mu\text{m}}^k$ (μJy)
S/N ≥ 4.5													
1	MM J104700.1+590109	3.7 \pm 0.8	4.1 \pm 0.6	3.5 $^{+0.6}_{-0.6}$	< 0.01	2.562 ^l	2.0	0.0025	278 \pm 6	490 \pm 11	687 \pm 72	0.0018	1280 \pm 9
2	MM J104627.1+590546	4.5 \pm 0.8	4.7 \pm 0.7	3.8 $^{+0.7}_{-0.7}$	< 0.01	4.29 ^m	3.0	0.037	35 \pm 6	49 \pm 23 ^t		0.11	41 \pm 6
3	MM J104631.4+585056	6.1 \pm 1.8	4.7 \pm 0.7	3.8 $^{+0.8}_{-0.7}$	< 0.01	1.8 ⁿ	0.5	0.0001^r	458 \pm 9	937 \pm 10	1633 \pm 85		
4	MM J104607.4+585413	2.8 \pm 0.8	3.2 \pm 0.5	2.7 $^{+0.5}_{-0.5}$	< 0.01	4.4 ⁿ	0.5	0.0025	29 \pm 3	50 \pm 11			
5	MM J104725.2+590339	4.9 \pm 0.9	5.2 \pm 0.8	4.0 $^{+0.8}_{-0.9}$	< 0.01	3.00 ^m	3.4	0.028	51 \pm 5	115 \pm 10		0.0099	395 \pm 26
6	MM J104638.4+585613	3.1 \pm 0.7	2.7 \pm 0.5	2.3 $^{+0.4}_{-0.4}$	< 0.01	2.03 ^o	2.1	0.0043	159 \pm 5	321 \pm 9	442 \pm 70	0.0074	662 \pm 8
7	MM J104700.1+585439	2.8 \pm 0.7	2.8 \pm 0.5	2.3 $^{+0.4}_{-0.4}$	< 0.01	4.2 ⁿ	2.0	0.016	41 \pm 4	60 \pm 10		0.10	329 \pm 18
8	MM J104633.1+585159	4.5 \pm 1.2	3.4 \pm 0.6	2.7 $^{+0.6}_{-0.6}$	< 0.01	3.3 ⁿ	0.4	0.0003	97 \pm 9	145 \pm 10		0.0022	342 \pm 8
9	MM J104704.9+585008	5.6 \pm 1.5	5.1 \pm 0.9	3.8 $^{+1.0}_{-0.9}$	< 0.01	3.9 ⁿ	0.6	0.0043^s	23 \pm 5	67 \pm 11			
10	MM J104622.9+585933	3.6 \pm 0.7	2.9 \pm 0.5	2.4 $^{+0.5}_{-0.5}$	< 0.01	2.6 ⁿ	2.1	0.0083	78 \pm 5	153 \pm 11	383 \pm 73	0.14	221 \pm 8
11	MM J104556.5+585317	3.5 \pm 0.9	3.4 \pm 0.6	2.7 $^{+0.6}_{-0.6}$	< 0.01	1.95 ^o	3.5	0.0057	314 \pm 10	427 \pm 9	662 \pm 74	0.017	684 \pm 7
12	MM J104448.0+590036	5.1 \pm 0.9	3.5 \pm 0.6	2.7 $^{+0.6}_{-0.7}$	< 0.01	2.16 ^m	3.0	0.0049	273 \pm 13	421 \pm 20	815 \pm 140	0.037	597 \pm 27
13	MM J104609.0+585826	2.7 \pm 0.7	2.7 \pm 0.5	2.1 $^{+0.5}_{-0.5}$	< 0.01	1.14 ^m	3.1	0.0067	197 \pm 3	461 \pm 10	1101 \pm 151	0.28	128 \pm 8
14	MM J104636.1+590749	4.3 \pm 0.8	4.3 \pm 0.8	3.0 $^{+0.9}_{-0.9}$	< 0.01	2.26 ^m	2.4	0.0079	97 \pm 3	215 \pm 14		0.0055	596 \pm 7
15	MM J104728.3+585213	5.1 \pm 1.1	4.5 \pm 0.9	3.0 $^{+0.9}_{-1.0}$	< 0.01	2.76 ^m	2.4	0.0044^r	180 \pm 15	245 \pm 12		0.0081	834 \pm 23
16	MM J104720.9+585151	2.3 \pm 1.0	3.8 \pm 0.7	2.7 $^{+0.8}_{-0.8}$	< 0.01	4.9 ⁿ	1.5	0.0088	47 \pm 6	55 \pm 15		0.13	307 \pm 9
17	MM J104610.4+590242	3.4 \pm 0.7	2.6 \pm 0.5	2.0 $^{+0.5}_{-0.5}$	< 0.01	4.0 ⁿ	1.1	0.0099^s	27 \pm 3	< 45		0.025	293 \pm 19
18	MM J104655.7+585000		4.6 \pm 0.9	2.9 $^{+1.1}_{-1.1}$	0.017	1.30 ^m	5.0	0.024	104 \pm 6	202 \pm 11 ^t	385 \pm 73	0.026	679 \pm 9
19	MM J104502.1+590404		2.6 \pm 0.5	2.0 $^{+0.6}_{-0.6}$	< 0.01	4.1 ⁿ	1.8	0.020	28 \pm 4	47 \pm 12			
20	MM J104617.0+585444		2.3 \pm 0.5	1.7 $^{+0.5}_{-0.5}$	< 0.01	> 4.6 ⁿ	5.0	0.12 ^s	15 \pm 4	< 33		0.027	67 \pm 8
21	MM J104530.3+590636		2.4 \pm 0.5	1.8 $^{+0.5}_{-0.5}$	< 0.01	3.1 ⁿ	0.9	0.0057	36 \pm 3	82 \pm 12		0.017	196 \pm 8
22	MM J104603.8+590448		2.7 \pm 0.6	2.0 $^{+0.6}_{-0.6}$	< 0.01	1.44 ^m	3.4	0.0094	165 \pm 5	355 \pm 15	485 \pm 72	0.019	595 \pm 9
23	MM J104641.0+585324		2.2 \pm 0.5	1.7 $^{+0.5}_{-0.5}$	< 0.01	3.6 ⁿ	1.6	0.016	31 \pm 4	56 \pm 12			
24	MM J104500.5+590731		2.4 \pm 0.5	1.8 $^{+0.6}_{-0.5}$	< 0.01	3.24 ^m	2.3	0.011	67 \pm 7	132 \pm 10		0.089	264 \pm 18
25	MM J104540.3+590347		2.3 \pm 0.5	1.7 $^{+0.6}_{-0.6}$	< 0.01	3.5 ⁿ	2.3	0.036	24 \pm 6	53 \pm 15		0.0071	119 \pm 7
26	MM J104522.8+585558		2.5 \pm 0.6	1.8 $^{+0.7}_{-0.6}$	< 0.01	> 5.0 ⁿ			< 14	< 40		0.11	239 \pm 20
27	MM J104702.4+585102		3.1 \pm 0.7	2.0 $^{+0.8}_{-0.9}$	0.018	2.9 ⁿ	0.2	0.0002	77 \pm 12	49 \pm 12		0.030	237 \pm 9
4.0 \leq S/N $<$ 4.5													
28	MM J104620.9+585434		2.1 \pm 0.5	1.5 $^{+0.5}_{-0.5}$	< 0.01	3.8 ⁿ	2.1	0.029^s	25 \pm 6	< 60			
29	MM J104556.1+590914		2.8 \pm 0.7	1.8 $^{+0.8}_{-0.8}$	0.022	0.044 ^p	4.7	0.0092	307 \pm 39	567 \pm 85		0.0012	4838 \pm 23
30	MM J104510.3+590408		2.2 \pm 0.5	1.5 $^{+0.6}_{-0.6}$	0.011	2.4 ⁿ	1.2	0.0034	74 \pm 6	155 \pm 10		0.012	56 \pm 7
31	MM J104624.7+585344		2.1 \pm 0.5	1.5 $^{+0.6}_{-0.5}$	< 0.01	2.90 ^m	2.9	0.027	43 \pm 3	72 \pm 9		0.079	236 \pm 7
32	MM J104539.6+585419		2.5 \pm 0.6	1.7 $^{+0.7}_{-0.7}$	0.023	2.40 ^q	5.2	0.056	46 \pm 3	113 \pm 9		0.059	485 \pm 7
33	MM J104535.5+585044		5.2 \pm 1.2	2.7 $^{+1.2}_{-1.2}$	0.20	3.7 ⁿ	6.3	0.049	70 \pm 9	101 \pm 10		0.19	245 \pm 7
34	MM J104453.7+585838		2.4 \pm 0.6	1.5 $^{+0.7}_{-0.7}$	0.022	3.5 ⁿ	3.0	0.031	40 \pm 8	65 \pm 10		0.13	76 \pm 7
35	MM J104717.9+585523		2.4 \pm 0.6	1.5 $^{+0.7}_{-0.7}$	0.025	3.71 ^m	2.4	0.014	60 \pm 5	68 \pm 11		0.099	297 \pm 23
36	MM J104608.1+590744		2.9 \pm 0.7	1.7 $^{+1.1}_{-0.9}$	0.052	4.5 ⁿ	2.1	0.041^s	16 \pm 3	< 47		0.11	396 \pm 39
37	MM J104610.8+585242		2.3 \pm 0.6	1.5 $^{+0.7}_{-0.7}$	0.030	1.72 ^q	2.3	0.0052	160 \pm 7	320 \pm 10	450 \pm 75	0.026	401 \pm 8
38	MM J104444.5+590817		2.8 \pm 0.7	1.5 $^{+0.9}_{-0.9}$	0.052	3.6 ⁿ	2.8	0.017	68 \pm 16	77 \pm 10		0.12	153 \pm 8
39	MM J104611.9+590231		2.1 \pm 0.5	1.4 $^{+0.7}_{-0.6}$	0.023	2.6 ⁿ	2.2	0.024^r	34 \pm 3	99 \pm 13		0.024	634 \pm 8
40	MM J104658.7+590633		3.0 \pm 0.8	1.5 $^{+1.2}_{-1.1}$	0.074	2.9 ⁿ	2.6	0.017	56 \pm 4	102 \pm 11		0.032	229 \pm 8
41	MM J104600.7+585502		2.1 \pm 0.5	1.4 $^{+0.7}_{-0.6}$	0.025	2.6 ⁿ	3.1	0.018	71 \pm 11	67 \pm 9			

NOTE.— P values in boldface type denote a likely counterpart ($P < 0.05$).

^aRaw flux density extracted from our “best” map (see §5.2).

^bRaw flux density extracted from our “full” map(see §5.2).

^cFlux density extracted from our “full” map, and corrected for flux boosting (see §5.6).

^dTotal probability that the deboosted flux density is ≤ 0 mJy (see §5.6)

^eAngular separation between MAMBO detection and 20 cm counterpart.

^fProbability of chance association with 20 cm counterpart.

^gFlux density of 20 cm counterpart (Owen & Morrison 2008).

^hFlux density of 50 cm counterpart (Owen et al. 2011a).

ⁱFlux density of 90 cm counterpart (Owen et al. 2009b).

^jProbability of chance association with 24 μ m counterpart.

^kFlux density of 24 μ m counterpart (Owen et al. 2011b).

^l z_{spec} from Polletta et al. (2006).

^m z_{phot} from Strazzullo et al. (2010).

ⁿ z_{α} estimated from Carilli & Yun (1999) spectral index (see §7.3).

^o z_{spec} from Fiolet et al. (2010).

^p z_{spec} from Owen & Morrison (2009a).

^q z'_{phot} from Magdis et al. (2010).

^rThere are two radio counterparts within 8'' of MAMBO source with $P < 0.05$; see Appendix A.

^sThe catalog of Owen & Morrison (2008) does not contain this radio counterpart (see §6.1).

^tFlux density is uncertain due to blending (see §6.2).

TABLE 3
1.2 MM NUMBER COUNTS

Flux Bin (mJy)	Differential		Integral	
	Flux Density (mJy)	dN/dS (deg ⁻² mJy ⁻¹)	Flux Density (mJy)	$N(> S)$ (deg ⁻²)
1.68–2.14	1.91	435 ⁺³⁶⁹ ₋₂₂₈	1.68	366 ⁺²¹² ₋₁₂₂
2.14–2.59	2.36	128 ⁺²⁰⁰ ₋₉₄	2.14	166 ⁺¹²⁸ ₋₆₃
2.59–3.05	2.82	156 ⁺¹⁵¹ ₋₈₉	2.59	108 ⁺⁹⁰ ₋₄₆
3.05–3.51	3.28	18 ⁺⁸⁰ ₋₁₇	3.05	37 ⁺⁵⁸ ₋₂₂
3.51–3.97	3.74	62 ⁺⁹⁷ ₋₄₅	3.51	28 ⁺⁴⁴ ₋₂₁

TABLE 4
AREA SURVEYED

Reference	Instrument	Field	Area (deg ²)	Depth (mJy beam ⁻¹)	HPBW (arcsec)
Greve et al. (2004)	MAMBO 1.2 mm	ELAIS-N2 & LH	0.099	0.8	11
Bertoldi et al. (2007)	MAMBO 1.2 mm	COSMOS	0.11	1.0	11
Scott et al. (2008)	AzTEC/JCMT 1.1 mm	COSMOS	0.15	1.3	18
Perera et al. (2008)	AzTEC/JCMT 1.1 mm	GOODS-N	0.068	0.96–1.16	18
Weiß et al. (2009)	LABOCA/APEX 870 μ m	ECDF-S	0.25	1.2	19.2
Austermann et al. (2010)	AzTEC/JCMT 1.1 mm	LHE & SXDF	0.5	1	18
Scott et al. (2010)	AzTEC/ASTE 1.1 mm	GOODS-S	0.14	0.48–0.73	30
Hatsukade et al. (2011)	AzTEC/ASTE 1.1 mm	AKARI, SXDF, & SSA	0.25	0.32–0.71	30
<i>This Work</i>	MAMBO 1.2 mm	LHN	0.16	0.75	11

TABLE 5
20 CM COUNTERPART IDENTIFICATION RATES

Reference	Instrument	Field	$\sigma_{1.4\text{GHz}}$ (μ Jy beam ⁻¹)	ID rate
Borys et al. (2004)	SCUBA 850 μ m	GOODS-N	9.0	58% (11/19)
Ivison et al. (2007)	SCUBA 850 μ m	LHE & SXDF	4.2 & 7	52% (62/120)
Bertoldi et al. (2007)	MAMBO 1.2 mm	COSMOS	8.5	73% (11/15)
Scott et al. (2008)	AzTEC 1.1 mm	COSMOS	10.5	44% (12/47)
Chapin et al. (2009)	AzTEC 1.1 mm	GOODS-N	4.5	76% (22/29)
Biggs et al. (2011)	LABOCA 870 μ m	ECDF-S	6.5	37% (47/126)
<i>This Work</i>	MAMBO 1.2 mm	LHN	2.7	93% (38/41)